Flow Field in a Single-Stage Model Air Turbine With Seal Rings and Pre-Swirled Purge Flow

by

Dennis M. Dunn

A Thesis Presented in Partial Fulfillment
of the Requirements for the Degree
Master of Science

Approved December 2010 by the
Graduate Supervisory Committee:

Kyle D. Squires, Chair
Ramendra P. Roy
Kangping Chen

ARIZONA STATE UNIVERSITY

December 2010

ABSTRACT

Modern gas turbines operate at high mainstream gas temperatures and pressures, which requires high durability materials. A method of preventing these hot gases from leaking into the turbine cavities is essential for improved reliability and cost reduction. Utilizing bleed-off air from the compressor to cool internal components has been a common solution, but at the cost of decreasing turbine performance. The present work thoroughly describes the complex flow field between the mainstream gas and a single rotor-stator disk cavity, and mechanisms of mainstream gas ingestion. A combined approach of experimental measurement and numerical simulation are performed on the flow in a single-stage model gas turbine. Mainstream gas ingestion into the cavity is further reduced by utilizing two axially overlapping seal rings, one on the rotor disk and the other on the stator wall. Secondary purge air is injected into the rotor-stator cavity pre-swirled through the stator radially inboard of the two seal rings. Flow field predictions from the simulations are compared against experimental measurements of static pressure, velocity, and tracer gas concentration acquired in a nearly identical model configuration. Operational conditions were performed with a main airflow Reynolds number of $7.86e4$ and a rotor disk speed of 3000rpm. Additionally the rotational Reynolds number was $8.74e5$ with a purge air nondimensional flow rate $c_w = 4806$. The simulation models a 1/14 rotationally periodic sector of the turbine rig, consisting of four rotor blades and four stator vanes. Gambit was used to generate the three-dimensional unstructured grids ranging from 10 to 20 million cells. Effects of turbulence were modeled using the single-equation Spalart-Allmaras as well as the realizable k-epsilon models. Computations were performed using FLUENT for both a simplified steady-state and subsequent time-dependent formulation. Simulation results show larger scale structures across the entire sector angle inside the cavity and certain unsteady mainstream ingestion mechanisms are realized from the tracer gas. Simulated velocity distributions were scrutinized against Particle Image Velocimetry plots in the rotor-stator cavity and are in reasonable agreement with all of the measurements.

ACKNOWLEDGMENTS

I would like to thank Dr. Squires and Dr. Roy for their guidance throughout writing this work. I would also like to thank Ding-Wei Zhou for helping with the experimental measurement acquisition, and Kringan Saha for help with technicalities of the Gambit and FLUENT software. Last, but not least, I would like to extend my gratitude to Solar Turbines Incorporated for their support that made this work possible.

TABLE OF CONTENTS

Page

SECTION

SECTION Page

SECTION Page

LIST OF FIGURES

LIST OF TABLES

NOMENCLATURE

b	outer radius of disk cavity [m], Figure 1
C	CO_2 tracer gas volumetric concentration (mass fraction)
C_{vax}	vane axial chord length [m]
$c_{w,fd}$	nondimensional free disk pumping mass flow rate, $= 0.219 \cdot Re_{\varphi}^{0.8}$
c_w	nondimensional mass flow rate of purge air, $= \dot{m}_{purge}/(\mu b)$
cfm	cubic feet per minute
D	diffusion coefficient [$m^2 s^{-1}$], Equation (68)
E	total specific energy content in fluid [J/Kg], Equation (75)
E_τ	empirical constant for y^+, =9.793, Equation (30)
F_k	k^{th} harmonic frequency [Hz], Equation (77)
g	gravitational acceleration, = 9.81 [$m \cdot s^{-1}$]
J	diffusion flux [$kg \cdot m^{-2} s^{-1}$], Equation (68)
K	turbulent kinetic energy [$m^2 s^{-2}$], Equation(35)
k	laminar thermal conductivity
k_t	turbulent thermal conductivity, Equation (75)
$\dot{m}$	mass flow rate [kg/s]
N	number of species in fluid mixture, Equation (70)
n	number of blades on rotor disk, Equation (77)
p	static pressure [Pa]
Q	volumetric Flow Rate [$m^3 \cdot s^{-1}$], Eq. 79
r	radial coordinate, $= \sqrt{y^2 + z^2}$ [m]
Re_φ	disk rotational Reynolds number, = $\rho \omega b^2 / \mu$
Re_{vax}	Main air flow Reynolds number, $= \rho V_{ax} C_{vax} / \mu$
rpm	revolutions per minute

S_{ij}	mean rate of strain tensor [s^{-1}], Equation (22)
Sc_t	Turbulent Schmidt number, Equation (69)
T	temperature [°C]
t	time [s]
U	blade hub speed, $= \underline{\omega} \times \underline{b}$ [m·s^{-1}]
V	Cell Volume [m^3]
V_2	actual velocity of main air at vane exit [m·s^{-1}]
V_φ	tangential velocity of air [m·s^{-1}]
V_r	radial velocity of air [m·s^{-1}]
V_x	axial velocity of air [m·s^{-1}]
$V_{ax} = V_{a2}$	mixed-mean axial velocity of main air in annulus [m·s^{-1}]
W	relative velocity of main air with respect to U [m·s^{-1}]
x	axial coordinate, measured upstream from the blade leading edge [m]
Y	species concentration (mass fraction), Equation (67)
y^*	dimensionless wall normal distance, Equation (64)
y^+	dimensionless wall normal distance, $= \frac{y_n \upsilon_\tau}{\nu}$
y_n	shortest wall distance to cell center [m], Equation (64)
α_2	angle to axial direction downstream, of the main air velocity just downstream of vane trailing edge [°]
β_2	angle to axial direction downstream, of the main air velocity relative to the blade velocity just downstream of vane trailing edge [°]
Δt	time step size [s]
δ_{ij}	Kronecker delta
ϵ	turbulent kinetic energy dissipation rate [m^{2}s^{-3}], Equation(35)
η	Kolmogorov length scale [m], Equation (8)
μ	dynamic viscosity [kg·m^{-1}s^{-1}]
ν	kinematic viscosity [$m^2 s^{-1}$]

$\tilde{\nu}$	eddy viscosity, Equation (23)
ν_t	turbulent eddy viscosity, Equation (24)
Ω	rotor disk rotational velocity [rpm]
ω	rotor disk rotational velocity [rad/s]
Ω_{ij}	rate of rotation tensor [s^{-1}], Equation (27)
φ	azimuthal coordinate [°]
ρ	density [kg$\cdot$m^{-3}]
σ_{ij}	stress tensor [Pa], Equation (4)
τ_w	wall shear stress $= \mu \frac{\partial u}{\partial x_n}$ [kg$\cdot$m^{-1}s^{-2}], Equation (32)
υ	fluid velocity [m$\cdot$s^{-1}]
υ_τ	friction velocity $= \sqrt{\frac{\tau_w}{\rho}}$ [m$\cdot$s^{-1}], Equation (32)
ζ	sealing effectiveness, Equation (80)

I. Introduction

Experimentation and simulation have been performed to gain a better understanding of the flow characteristics within a single turbine stage and to assess the accuracy of the simulation predictions - specifically the flow characteristics in the main-gas path, the rotor-stator cavity, and the interaction of these two regions through the seal rings. Unsteady interactions between the rotor blades and stator vanes are a major cause of mainstream gas ingestion into the rotor-stator cavity. Non-uniform circumferential static pressure distributions in conjunction with the time-dependent interactions lead to instabilities that cause ingestion. As a consequence, this may cause undesired thermal fatigue, overheating, and thermal expansion of the turbine materials, thus purge air injection is a commonly employed solution to overcome ingestion.

In modern gas turbine applications, approximately twenty percent of the incoming compressed air is used for secondary air systems.[3] Though cooling and sealing flows are only a fraction of that total, it is still desirable to reduce the secondary system usage as much as possible. Turbine rotor-stator cavities are an essential link between the neighboring rotating and stationary wall sections within any turbine configuration. Preventing hot mainstream gases from entering these cavities is of great importance from a reliability standpoint. Turbine rotor components experience more mechanically demanding conditions than the neighboring stator counterparts. Temperatures in the main gas path typically operate between 900 - 1300$^\circ C$, and so the internal components would be very expensive if required to operate at these same temperatures. Normal practice is to maintain the internal disk and hub components to less than 500°C.[4]

Purge air injected into the cavity serves to cool the rotor disk in addition to countering main gas ingestion with. These secondary flows are also known as cooling or sealing flows respectively. Protruding seal rings on the cavity walls are a supplemental method of reducing ingestion and the design of a labyrinth seal may help reduce the ingestion and secondary flow requirements. Turbine efficiency is directly improved by minimizing the usage of purge air for two reasons. Firstly, by allowing more main-stream air for combustion, and secondly, by reducing the flow blockage created by egressed air flowing into the path of the mainstream gas. Demand is always being placed on increasing pressures, temperatures, and rotation speeds to boost the engine thrust-to-weight ratios in aircraft turbines,[5] thus making secondary flow and seal designs very critical aspects of turbine design.

A. Scope

The present contribution aims to examine, experimentally and numerically, the complex flow field in the rotor-stator cavity along with the mechanisms behind mainstream ingestion and sealing effectiveness. Comparisons can be made between the experiments and simulations to determine the accuracy of the computer models. The present configuration employs the use of two axially overlapping seal rings, of which, one is attached to the stator wall and the other to the rotor disk, producing a small radial gap (2.5 mm) between them. Both seal rings are located radially inboard of the disk rim and pre-swirled purge air is injected into the cavity radially inboard of the seal rings, not through the hub as in many previous experiments.[2,6–13] Boundary conditions were configured such that 80% of the incoming purge flow is forced out through the narrow seal ring gap and into the main gas flow, while the remaining 20% exits through the outlet at the hub.

A single experimental configuration was analyzed and discussed for which two different CFD simulation results are presented. FLUENT 6.3 (2008) was used to simulate a further-simplified model of the experimental setup for comparison. Simulations performed in the present work aim to keep the resolution refined and simulate flow structures that are not attainable with the single blade/vane setup. They also offer supplemental flow field results that are difficult or impossible to measure experimentally. Certain measurements of static pressure, tracer gas concentration, and cavity fluid velocity were obtained in the experimental setup for comparison and are presented. Simulation results obtained show that larger scale time-dependent flow structures evolve, but are restricted by the periodic four vane – four blade domain size.

Two main goals are presented in the current contribution. First, an attempt is made to determine whether a simulation in FLUENT can closely predict the flow characteristics measured in an experimental model turbine rig. Secondly, the results from the experiments and simulations are used to gain a better understanding of factors leading to ingestion. The present work was also published in an ASME paper[14] and many of the same plots were used.

B. Background

The predominant cause of ingestion is known to be the three-dimensional unsteady flow field that exists in the main gas path of turbine stage.[2,6–9] Accordingly, experiments and computational fluid dynamic (CFD) simulations have been performed to better understand the ongoing physical processes. Some previous CFD simulations by Roy *et al.*,[2,10] Zhou *et al.*[6] and Teramachi *et al.*[7] used configurations containing only a single pitch of the blade and vane. Jakoby *et al.*[11] used sectors containing two vanes and Okita *et al.*,[15] Zerelli *et al.*,[3] and Gentilhomme *et al.*[16] used a two-blade sector.

All of these previous sector model simulations were unable to resolve the larger structures that form over a multitude of vanes, but showed ingestion nonetheless. Unsteady simulations of full 360 degree turbine geometries have also been performed by Cao *et al.*,[8] and Jakoby *et al.*,[11] but at the cost of incorporating additional simplifications. For example, none had modeled the blades/vanes in the main gas path, and focused solely on the cavity using lower resolution grids. It was shown that unsteady effects were still present, independent of blade passing events, and still caused ingestion. To measure the ingestion, Jakoby *et al.*used air as both the main and tracer gas, but made them distinguishable in FLUENT.

Teramachi *et al.*[7] and Hills *et al.*[12] employed a sliding interface method for solving unsteady models, also replacing the rotor blades with struts to verify that the presence of blades did indeed degrade sealing effectiveness. Okita *et al.*[15] placed emphasis on developing a labyrinth seal configuration to significantly reduce purge air usage by reducing turbulent mixing within the cavity. It was shown that it is possible to localize the cooling to the rotor side by reducing the turbulent mixing within the cavity.

Paniagua *et al.*[17] investigated the effects of the ejected purge flow blocking the transonic mainstream flow and altering the velocity triangles. As a result, the rotor relative incidence is altered, affecting the turbine performance; McLean *et al.*[18,19] also reached this conclusion. They concluded that the cavity flow and ejected purge flow into the mainstream must be considered during the preliminary design phase to accurately predict the mainstream gas behavior. This supplements the importance of decreasing the purge flow rate as much as possible. Furthermore, Denton *et al.*[20] emphasizes the importance of modeling both the main and secondary flow cycles together with a precise 3D geometry in a CFD simulation to completely capture the unsteady phenomena. Denton also states that CFD modeling has been the most critical breakthrough in modern turbo machinery design.

Bricaud *et al.*[21] also performed PIV measurements on a pre-swirled turbine setup. Findings showed that the pre-swirler can introduce turbulence and losses by creating high velocity gradients at the shear layers of the jets. Pre-swirlers could be improved by using more nozzles to reduce the spacing between them or by even using a set of secondary guide vanes instead of nozzles to inject the pre-swirled flow.

II. Experimental Apparatus

Before the simulations were performed, a research team led by Dr. Roy at ASU carried out a series of experiments and measurements on a model turbine rig. A corresponding simulation was designed to match the turbine configuration and compare the results. The radial-axial cross-section schematic of the turbine configuration shown in Figure 1 was used to design the 3D SolidWorks model.

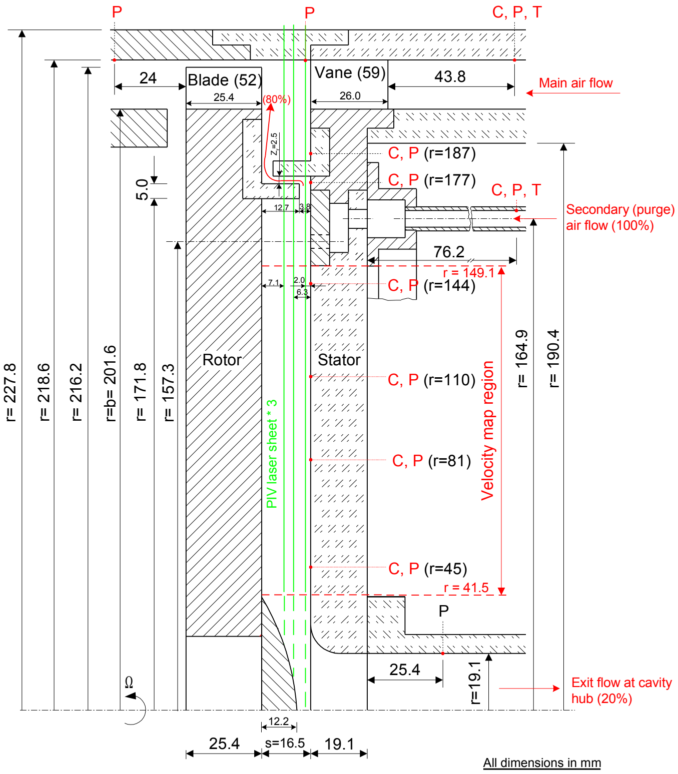

Figure 1. Axial-Radial schematic diagram - C: Concentration tap; P: Static pressure tap; T: Thermocouple

Pre-swirled purge air is injected from the stator side into the rotor-stator cavity. The purge air is supplied to the cavity through 30 circular holes of 4.76 mm diameter at a radius of 157.3 mm, each hole being equally spaced circumferentially. The air

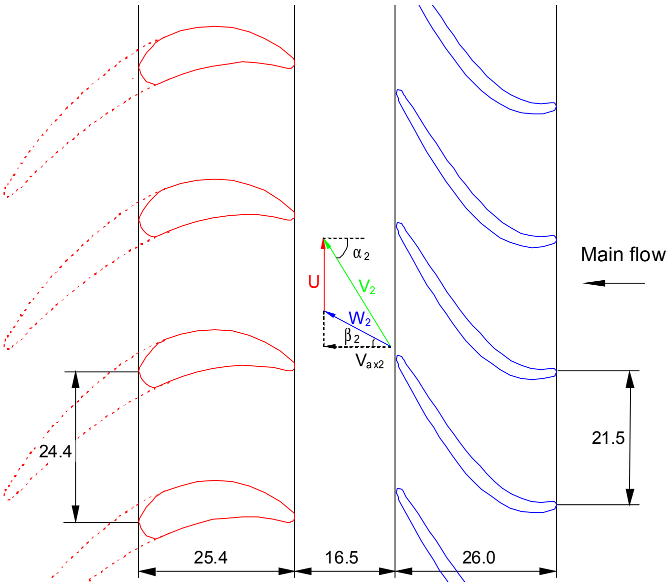

Figure 2. Velocity diagram of main air flow and the vane/blade geometry

is injected at an angle of 10 degrees from the stator surface in the axial-tangential plane. These purge nozzles are oriented so that the tangential velocity imparted to the purge air is in the direction of the rotor rotation. A second schematic of the axial-azimuthal (x-φ) plane shows the vane and blade geometries in Figure 2. There are 59 partial-height, full-length ($C_{vax} = 26$ mm) vanes (often also referred to as Nozzle Guide Vanes, NGV) which turn the incoming main air flow by α_2 =60.1 degrees. The aluminum rotor disk is 403.2 mm in diameter and has 52 partial-height, partial-length blades. Partial heights and partial lengths were used to reduce the pumping power requirements. The two seal rings provide an axially overlapping radial clearance seal configuration.

Table 1 lists the experimental conditions supplied to the model turbine rig. 20 percent of the purge flow air exits through the purge outlet at the rotor hub while the remaining 80 percent egressed through the seal rings and into the mainstream flow. The cavity hub outflow rate was maintained with three dry-vacuum pumps operating in parallel, each having a maximum flow rate of 12 cfm (0.006 m^3/s) and a maximum vacuum of 25.5" Hg (86.4 kPa). The hub air flow was drawn out such that the disk cavity pressure was maintained.

A. Static Pressure Measurement

To measure the time-average static (gage) pressure, a differential pressure transducer-digital manometer-Scanivalve set-up was used. Pressure taps were placed on the stator wall inside the cavity, between the seal rings, and on the outer shroud in the main gas path. Figure 1 shows the locations of the six pressure taps on the stator wall. At the outer shroud radius, $r = 218.6$ mm ($r/b = 1$), sixteen taps were provided circumferentially over one vane pitch. The pressure tap positions on the outer shroud and stator seal can be found in Ref. 2 and shown in Figure 3. The uncertainty in these pressure measurements is ± 2 percent based on the instrument and data acquisition uncertainties.

B. CO_2 Measurement

Because of the unsteady ingress phenomenon, a useful measure of ingestion is to seed indigenous cavity air with a tracer gas. In the present work, carbon dioxide (CO_2) was used. A subsequent measurement of CO_2 concentration will determine the extent of mixing between the mainstream and cavity air. A constant 4 percent volumetric concentration (mass fraction) of CO_2 was injected through the purge air and was monitored just upstream of its entrance to the disk cavity to ensure

Table 1. The Experimental and Simulation Boundary Conditions

Main air flow rate (cfm / Re_{vax})	$2100/7.86\times10^4$
Rotor speed (rpm/Re_{φ})	$3000/8.74\times10^5$
Free disk pumping flow rate (cfm / $c_{w,fd}$)	$77.4/12404$
$\beta_2[°]$	14.2
Purge air flow rates (c_w)	
Total supplied	4806
Outflow at cavity hub	961
Egress to main flow	3845

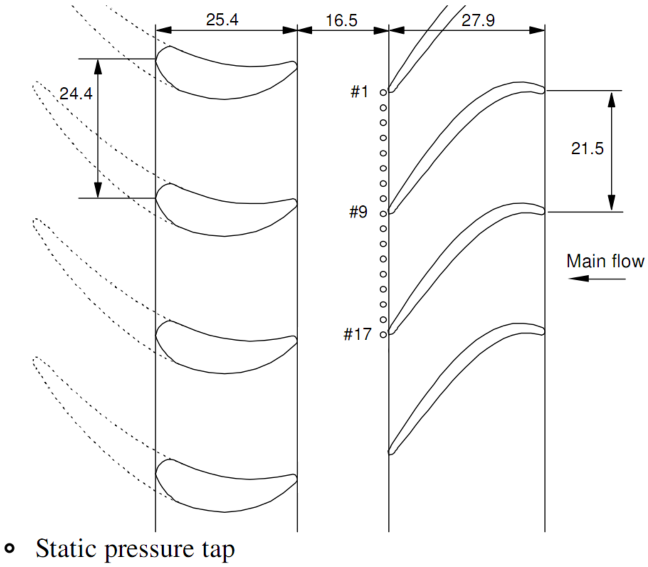

Figure 3. Axial-Azimuthal (x-φ) schematic of pressure tap locations

the introduced air-CO_2 mixture remained at that constant volumetric concentration. This particular CO_2 volumetric concentration was chosen because it has been used successfully in many earlier works.[2,6,13] The radial locations of sampling tubes on the stator disk are shown in Figure 1, note that they are the same as the six pressure tap locations. The CO_2 concentration was also monitored in the main air to serve as reference and measured by a NDIR gas analyzer. Measured CO_2 volumetric concentrations have an uncertainty of ± 0.11 percent and the values were time-averaged over many rotor revolutions, but are local with respect to the vane position and radial coordinate.

C. Air velocity vector maps

The final measurements consisted of using a dual Nd:YAG laser (Spectra-Physics PIV-200) providing short pulses (≅10 ns width) of 532 nm (green) light to illuminate seed particles (olive oil droplets, 1-2 μm) in the rotor-stator cavity flow. The droplets were generated by means of a Laskin nozzle, and the light sheet optics system produced a light sheet in the radial-azimuthal (r-φ) plane of about 351 mm height and 70.7 μm thickness at its waist. Figure 1 shows the axial locations of the three various laser planes, the light sheet was introduced through the transparent and optically polished outer shroud. Images were captured by means of a high-resolution CCD camera (2048 × 2048 pixels) through the transparent and optically polished stator wall. The light sheet and camera could be accurately positioned by means of a three-dimensional traverse equipped with a rotary stage.

III. The Navier-Stokes Equation

A common approach to performing Computational Fluid Dynamics involves solving the Navier-Stokes equations numerically. The following derivations are a compilation of information from Refs. 1, 22, 23, and 24. Beginning with the continuity equation for a general fluid continuum in Einstein notation,

$$\frac{\partial \rho}{\partial t} + \frac{\partial}{\partial x_i}(\rho \upsilon_i) = 0 \tag{1}$$

Here υ_i corresponds to the Cartesian velocity components in $\mathcal{R}^3$ for $i = 1, 2, 3$ such that the vector $\underline{\upsilon} = [\upsilon_1, \upsilon_2, \upsilon_3]^T$, and x_i corresponds to the Cartesian coordinate directions. For an incompressible fluid, i.e. constant density ρ, Equation (1) simplifies to

$$\frac{\partial \upsilon_i}{\partial x_i} = \nabla \cdot \underline{\upsilon} = 0 \tag{2}$$

which can be physically interpreted as the fluid velocity field having no sources or sinks, i.e. the divergence of velocity is zero. The differential form of the momentum equation is written as,

$$\rho \left(\frac{\partial \upsilon_i}{\partial t} + \upsilon_j \frac{\partial \upsilon_i}{\partial x_j} \right) = \frac{\partial \sigma_{ij}}{\partial x_j} + \rho g_i \tag{3}$$

and is derived from the total derivative of velocity and Newton's second law of motion. Correspondingly, written as $dm(\frac{D\upsilon_i}{Dt}) = \Sigma(dF)$ reveals the origin of the time dependent and convective acceleration terms on the left-hand side. After dividing through by infinitesimal fluid volume dV, the density $\rho = \frac{dm}{dV}$ appears and the equation is balanced by the body forces $\frac{dF}{dV}$ on the right hand side, such as the divergence of stresses $\nabla \cdot \sigma_{ij}$. Gravity body forces g_i are neglected from the remainder of the present work. Equations (1) and (3) are the continuity and momentum equations respectively, and are solved together to predict the flow field. The energy Equation (76) is described later and can be used in conjunction to solve additional flow state-variables. Here σ_i is the stress tensor which is a combination of stresses using the constitutive law for incompressible fluids,

$$\sigma_{ij} = -p\delta_{ij} + \tau_{ij} \tag{4}$$

where p is the static pressure and δ_{ij} is the Kronecker delta. Here τ_{ij} is the deviatoric part of the stress tensor defined as,

$$\tau_{ij} = \mu \left(\frac{\partial \upsilon_i}{\partial x_j} + \frac{\partial \upsilon_j}{\partial x_i} \right) \tag{5}$$

Replacing the decomposed stresses into Equation (3) yields

$$\rho \left(\frac{\partial \upsilon_i}{\partial t} + \upsilon_j \frac{\partial \upsilon_i}{\partial x_j} \right) = -\frac{\partial p}{\partial x_i} + \frac{\partial \tau_{ij}}{\partial x_j} \tag{6}$$

This is the general Navier-Stokes equation where τ_{ij} for a Newtonian fluid is the deviatoric stress portion, and may also be written in any of the following common forms[23]

$$\frac{\partial \tau_{ij}}{\partial x_j} = \mu \frac{\partial}{\partial x_j}\left(\frac{\partial \upsilon_i}{\partial x_j} + \frac{\partial \upsilon_j}{\partial x_i}\right) = \mu \frac{\partial^2 \upsilon_i}{\partial {x_j}^2} = \mu \nabla^2 \upsilon_i \tag{7}$$

where $\nabla^2 \upsilon \equiv \nabla \cdot (\nabla \upsilon) = \frac{\partial^2 \upsilon}{\partial x_j^2}$ is the Laplace operator. Together the continuity and momentum equations, (2) and (6) respectively, can be coupled together with adequate (closed) boundary conditions to solve for the state variables: pressure p and velocity υ_i.

Numerical simulation can be carried out using the Navier-Stokes Equation (6) on finite fluid volumes, but the scale of the discretized mesh must be on the same order as the smallest flow structures that are to be resolved. This method is known as Direct Numerical Simulation (DNS) and proves to be very inefficient because it requires the grid spacing to be on the order of the Kolmogorov length scale,[24] defined as

$$\eta \equiv \left(\frac{\nu^3}{\epsilon}\right) \tag{8}$$

The computing requirements to model the required fine grid size will not be practical in most engineering applications for many more decades. As explained in the next segment, this issue is overcome by not resolving the fluid to it's smallest scale structures, but instead, assumptions are made about the small scale ”‘turbulent”’ motions and additional turbulence models are introduced to close the new governing equations.

A. Time Averaging

A useful approach is to employ time averages over short time periods where higher frequency fluctuations will be segregated from larger flow behavior. One flow modeling assumption is to treat the velocity vectors as consisting of a mean (time-average) and fluctuating component. This effectively groups the small scale fluctuations into a single value (adding an additional state-variable), and does not require that the fluid mesh be fine enough to resolve those small turbulent scales. The time averaging method is known as Reynolds Averaging, and performing this operation on a flow state-variable such as υ_i is defined as,

$$\bar{\upsilon}_i \equiv \frac{1}{\Delta t} \int_{t_o}^{t_o + \Delta t} \upsilon_i dt \tag{9}$$

A time-averaged mean value is represented by an overbar, e.g. $\bar{\upsilon}_i$. The period Δt is chosen appropriately such that small scales (high frequency) fluctuations are averaged-out, but not too large either, so that the important larger scale unsteady flow features remain. It follows then that the decomposition of any state variable is analogous to

$$\upsilon_i = \bar{\upsilon}_i + \upsilon_i' \tag{10}$$

where υ' is the time-dependent fluctuating value written in Cartesian coordinates as $\underline{\upsilon}' = [\upsilon_1', \upsilon_2', \upsilon_3']^T$. The decomposition proves useful because of the following properties and identities for any arbitrary time-dependent variables f and g,

$$\begin{gathered}\bar{f}' = 0 \qquad \overline{f'f'} \neq 0 \qquad \overline{f'g'} \neq 0 \qquad \overline{\bar{f}g'} = 0 \qquad \overline{\bar{f}g} = \bar{f}\bar{g} \\ \overline{f+g} = \bar{f} + \bar{g} \qquad \overline{(\bar{f}+f')^2} = \bar{f}^2 + \bar{f'}^2\end{gathered} \tag{11}$$

most notably that the average of a fluctuation multiplied by a scalar is zero. However, note that the average of two fluctuations multiplied together is non-zero. This non-linear term leads to closure problems and gives rise to turbulence modeling as described next. Reynolds proposed substituting the decomposed variables into the Navier-Stokes and continuity equations, leading to the Reynolds-Averaged Navier-Stokes (RANS) equations. For the continuity equation thus yields,

$$\frac{\partial \bar{\rho}}{\partial t} + \frac{\partial}{\partial x_j}(\bar{\rho}\bar{\upsilon}_j + \overline{\rho' \upsilon_j'}) = 0 \tag{12}$$

For incompressible flows, the density fluctuations ρ' are zero because the density is assumed constant ($\frac{\partial \rho}{\partial t} = 0$ and $\rho = \bar{\rho}$) so the continuity equation becomes,

$$\frac{\partial \bar{\upsilon}_j}{\partial x_j} = \nabla \cdot \underline{\bar{\upsilon}} = 0 \tag{13}$$

Subtracting Equation (2) from Equation (13) yields

$$\frac{\partial \upsilon_i'}{\partial x_i} = \nabla \cdot \underline{\upsilon}' = 0 \tag{14}$$

meaning that the velocity's fluctuating component must also independently satisfy the continuity equation. Likewise, substituting the decomposed state-variables into the Navier-Stokes equation gives

$$\begin{aligned}\frac{\partial}{\partial t}\Big(\bar{\rho}\bar{\upsilon}_i + \overline{\rho'\upsilon'_i}\Big) &+ \frac{\partial}{\partial x_j}\Big(\bar{\rho}\bar{\upsilon}_i\bar{\upsilon}_j + \bar{\upsilon}_i\overline{\rho'\upsilon'_j}\Big) \\ &= -\frac{\partial \bar{p}}{\partial x_i} + \frac{\partial}{\partial x_j}\Big(\bar{\tau}_{ij} - \bar{\upsilon}_j\overline{\rho'\upsilon'_i} - \bar{\rho}\overline{\upsilon'_i\upsilon'_j} - \overline{\rho'\upsilon'_i\upsilon'_j}\Big)\end{aligned} \tag{15}$$

However, adhering to the incompressible flow assumption allows setting the density fluctuations $\rho' = 0$, and the RANS momentum equation reduces to a much simpler form,

$$\frac{\partial}{\partial t}(\rho\bar{\upsilon}_i) + \frac{\partial}{\partial x_j}(\rho\bar{\upsilon}_i\bar{\upsilon}_j) = -\frac{\partial \bar{p}}{\partial x_i} + \frac{\partial}{\partial x_j}(\bar{\tau}_{ij} - \rho\overline{\upsilon'_i\upsilon'_j}) \tag{16}$$

where $\bar{\tau}_{ij}$ becomes,

$$\bar{\tau}_{ij} = \mu\left(\frac{\partial \bar{\upsilon}_i}{\partial x_j} + \frac{\partial \bar{\upsilon}_j}{\partial x_i}\right) \tag{17}$$

The RANS momentum Equation (16) can be rewritten as

$$\frac{\partial \bar{\upsilon}_i}{\partial t} + \bar{\upsilon}_j\frac{\partial \bar{\upsilon}_i}{\partial x_j} = -\frac{1}{\rho}\frac{\partial p}{\partial x_i} + \nu\nabla^2\bar{\upsilon}_i - \frac{\partial \overline{\upsilon'_i\upsilon'_j}}{\partial x_j} \tag{18}$$

by dividing through all terms by density ρ, where $\nu = \mu/\rho$ is the kinematic viscosity.

B. The Reynold’s Stress

The closure problem arises in the RANS equation (18) because of the non-linear term $\overline{\upsilon_i'\upsilon_j'}$ from the convective acceleration, known as the Reynolds stress

$$R_{ij} = \overline{\upsilon_i'\upsilon_j'} \tag{19}$$

Closing the RANS equation requires additional modeling to solve for this Reynold’s stress R_{ij}. Here the Boussinesq hypothesis is applied to model the Reynolds stress term from Equation (18). Note that a new proportionality constant $\nu_t > 0$, the turbulent eddy viscosity, has been introduced. Models of this type are known as eddy viscosity models or EVM’s.

$$-\overline{\upsilon_i'\upsilon_j'} = \nu_t \left(\frac{\partial \bar{\upsilon}_i}{\partial x_j} + \frac{\partial \bar{\upsilon}_j}{\partial x_i} \right) - \frac{2}{3} \left(K + \nu_t \frac{\partial \bar{\upsilon}_k}{\partial x_k} \right) \delta_{ij} \tag{20}$$

The Boussinesq hypothesis is used for the Spalart-Allmaras (S-A), k-ϵ, and k-ω models and offers a relatively low cost computation for the turbulent viscosity ν_t. The S-A model uses only one additional equation to model turbulent viscosity transport. In 1887 Boussinesq proposed relating the turbulent stresses to the mean flow to close the system of equations. Thus, Boussinesq’s proposed method of using an eddy viscosity to solve for the Reynold’s stress can be simplified from Equation

(20) for incompressible flow,

$$-R_{ij} = -\overline{\upsilon_i'\upsilon_j'} = 2\nu_t S_{ij} - \frac{2}{3}K\delta_{ij} \tag{21}$$

because the divergence term $\frac{\partial \bar{\upsilon}_k}{\partial x_k} = 0$ in incompressible flows. This Equation will be used for the time averaged incompressible governing equations to compute the Reynold's stress for all of the turbulence models described in the present work. ν_t is the eddy viscosity, S_{ij} is the mean rate of strain tensor, and K is the turbulent kinetic energy. K is only used in the two-equation models section and will be defined there, whereas the one-equation models will ignore the K term. The mean rate of strain tensor is defined as,

$$S_{ij} = \frac{1}{2}\left(\frac{\partial \bar{\upsilon}_j}{\partial x_i} + \frac{\partial \bar{\upsilon}_i}{\partial x_j}\right) \tag{22}$$

C. Pressure-Velocity Coupling

To reiterate, the continuity and momentum equations are used together to solve for the state variables: pressure p and velocity υ_i for each cell in the mesh. The pressure-based solver was used throughout all simulations in the present work. Thus, FLUENT offers two methods to calculate the solution in a pressure-based solver scheme: segregated and coupled. The coupled solver converges more quickly, but requires 1.5-2 times as much memory as the segregated method because the pressure correction equation solves the continuity and momentum equations in a closely-coupled manner.[1] In the present work, only the segregated solvers SIMPLE and PISO (Pressure-Implicit with Splitting of Operators)[1] were used.

First the fluid properties such as density, viscosity, and specific heat are computed by the solver. Then, depending on the method chosen, the momentum equation and a pressure correction equations are either solved coupled or individually (sequentially) to solve for velocity and pressure. The PISO method performs additional loops internally (skewness-neighbor coupling) that help the calculated values satisfy the momentum and continuity equations more accurately. Lastly, the species, temperature, turbulence, and other scalar equations are solved as described in the next two sections. Figure 4 shows the flow chart diagram for the different schemes.

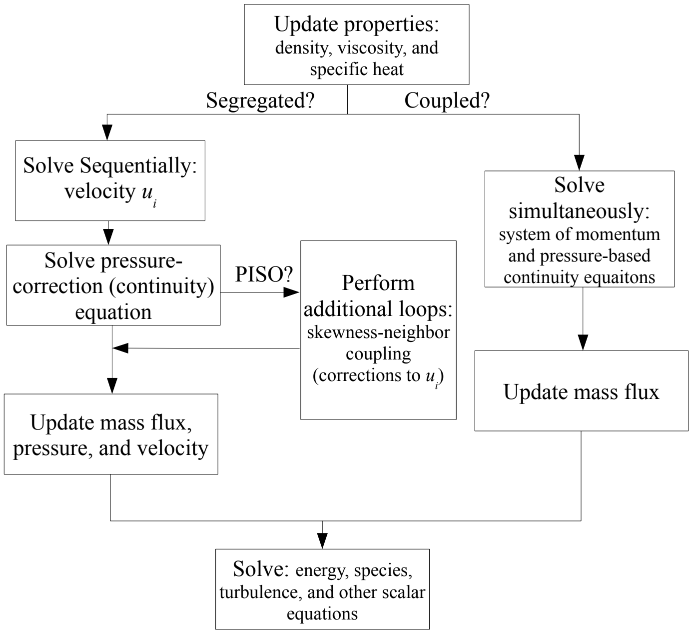

Figure 4. Flow chart of pressure-velocity correction schemes, modified from Ref. 1

IV. Modeling Turbulence

Three different classes of eddy viscosity models exist: zero-equation (algebraic), one-equation, and two-equation models. The names imply the number of differential equations required in addition to the fundamental RANS differential equation. Zero-equation models close the RANS equations using only algebraic relations, i.e. the nonlinear term such as the Reynolds stress is solved using algebraic relationships to the mean flow variables. Some zero-equation models include Prandtl's Mixing Length, the Cebeci-Smith, and the Baldwin-Lomax models.[25] Common one-equation models include the Baldwin-Barth and Spalart-Allmaras models.[25] Common two-equation models include the k-ϵ, k-ω, and Menter's Shear Stress Transport models.

The Spalart-Allmaras is the simplest model available in FLUENT and an example of a one-equation model. The k-ϵ and k-ω models are also offered in FLUENT. Many higher order models exist such as the SST and LES, but they are beyond the scope of this paper. The present work employs the S-A model and the k-ϵ models only, and they will be discussed in great detail. All of the models share a common trait in that they usually include proportionality constants (when relating the mean flow variables) determined by experimentation, empiricism, and/or dimensional analysis. The information presented here is a culmination of information from FLUENT,[1] Davidson[26] and Bernard.[22]

A. Spalart-Allmaras Model

The Spalart-Allmaras (S-A) model was used during the present work for MESH I. The proposed model uses one additional differential equation to solve for the transport of a modified turbulent eddy viscosity $\tilde{\nu}$. This quantity is identical to the turbulent kinematic viscosity ν except in the near wall regions where FLUENT employs certain wall functions to modify $\tilde{\nu}$. Note that the last term in the Boussinesq assumption, Equation (20), is ignored when computing the Reynolds stress because the kinetic energy K is not calculated. The model was developed using empiricism and dimensional analysis with the working variable $\tilde{\nu}$, known as the eddy viscosity. Its transport equation takes the form,

$$\frac{D\tilde{\nu}}{Dt} = c_{b1}\tilde{S}\tilde{\nu} - c_{w1}f_w\left(\frac{\tilde{\nu}}{d}\right)^2 + \frac{1}{\sigma_{\tilde{\nu}}}\Big[\frac{\partial}{\partial x_j}\left\{(\nu+\tilde{\nu})\frac{\partial\tilde{\nu}}{\partial x_j}\right\} + c_{b2}(\frac{\partial\tilde{\nu}}{\partial x_j})^2\Big] \tag{23}$$

where $c_{b1}\tilde{S}\tilde{\nu}$ is the production term, $(1/\sigma_{\tilde{\nu}})[\nabla\cdot((\nu+\tilde{\nu})\nabla\tilde{\nu}) + c_{b2}(\nabla\tilde{\nu})^2]$ is the diffusion term, and $[c_{w1}f_w][\tilde{\nu}/d]^2$ is the destruction term of turbulent viscosity. The turbulent eddy viscosity ν_t is computed using,

$$\nu_t = \tilde{\nu}f_{v1}, \qquad f_{v1} = \frac{\chi^3}{\chi^3 + c_{v1}^3}, \qquad \chi = \frac{\tilde{\nu}}{\nu} \tag{24}$$

where ν is the molecular viscosity and f_{v1} is a damping function. In the production term, the modified vorticity, $\tilde{S}$, is written as,

$$\tilde{S} = S + \frac{\tilde{\nu}}{\kappa^2 d^2} f_{v2}, \qquad f_{v2} = 1 - \frac{\chi}{1 + \chi f_{v1}} \tag{25}$$

where S is the revised vorticity magnitude:

$$S \equiv |\Omega_{ij}| + C_{prod} \text{min}(0, |S_{ij}| - |\Omega_{ij}|) \tag{26}$$

and $|\Omega_{ij}| \equiv \sqrt{2\Omega_{ij}\Omega_{ij}}$ is the magnitude of mean rate-of-rotation tensor defined by

$$\Omega_{ij} = \frac{1}{2}\left(\frac{\partial \bar{\upsilon}_i}{\partial x_j} - \frac{\partial \bar{\upsilon}_j}{\partial x_i}\right) \tag{27}$$

In the destruction term, the function f_w is defined as,

$$f_w = g\left[\frac{1 + c_{w3}^6}{g^6 + c_{w3}^6}\right]^{1/6}, \qquad g = r + c_{w2}(r^6 - r), \qquad r = \frac{\tilde{\nu}}{\tilde{S}\kappa^2 d^2}. \tag{28}$$

The constants appearing in the above equations have the default values in FLUENT of

$$c_{b1} = 0.1355, \qquad c_{b2} = 0.622, \qquad \sigma_{\tilde{\nu}} = 2/3, \qquad c_{v1} = 7.1, \qquad \kappa = 0.4187,$$

$$c_{w1} = c_{b1}/\kappa^2 + (1 + c_{b2})/\sigma_{\tilde{\nu}}, \qquad c_{w2} = 0.3, \qquad c_{w3} = 2, \qquad c_{v1} = 7.1.$$

To handle the wall boundaries, the Dirichlet wall boundary condition sets $\tilde{\nu} = 0$, and when the mesh is fine enough to resolve the laminar sublayer then the following relation is used to calculate the wall shear stress,

$$\frac{\bar{\upsilon}}{\upsilon_\tau} = \frac{\upsilon_\tau y_n}{\nu} \tag{29}$$

otherwise if the mesh is too coarse, then the log law of the wall is employed

$$\frac{\bar{\upsilon}}{\upsilon_\tau} = \frac{1}{\kappa}\text{ln}E_\tau \left(y_n \frac{\upsilon_\tau}{\nu} \right) \tag{30}$$

where υ is the velocity parallel to the wall, υ_τ is the shear velocity, y_n is the normal distance from the wall, $\kappa = .4187$ is the von Karman Constant, and $E_\tau = 9.793$ is the Empirical constant. For convenience, FLUENT defines the non-dimensionalized parameters,

$$\upsilon^+ = \frac{\bar{\upsilon}}{\upsilon_\tau} \qquad y^+ = \frac{y_n \upsilon_\tau}{\nu} \tag{31}$$

The friction velocity υ_τ is defined as,

$$\upsilon_\tau = \sqrt{\frac{\tau_w}{\rho}} \tag{32}$$

where $\tau_w = \mu \frac{\partial u}{\partial x_n}$ is the wall shear stress.

B. Standard k-epsilon Model

The standard K-ϵ two-equation model commonly used in modern engineering applications uses the following two additional differential equations to close the RANS equation,

$$\frac{\partial K}{\partial t} + \bar{\upsilon}_j \frac{\partial K}{\partial x_j} = \mathcal{P} - \epsilon + \nu \nabla^2 K - \frac{\partial}{\partial x_i}\left(\frac{\overline{p\upsilon'_i}}{\rho} + \overline{\upsilon'_i(\upsilon'^2_j/2)} \right) \tag{33}$$

$$\frac{\partial \epsilon}{\partial t} + \bar{\upsilon}_j \frac{\partial \epsilon}{\partial x_j} = P^1_\epsilon + P^2_\epsilon + P^3_\epsilon + P^4_\epsilon + \Pi_\epsilon + T_\epsilon + D_\epsilon - \Upsilon_\epsilon \tag{34}$$

where K is the turbulent kinetic energy and ϵ is the turbulent kinetic energy dissipation rate. The buoyancy and compressibility production terms are ignored and not shown. K represents the kinetic energy contained in the fluctuating velocity term, from the decomposition,

$$\frac{1}{2}\overline{\upsilon^2_i} = \overline{K} + K = \frac{1}{2}\overline{\upsilon_i}^2 + \frac{1}{2}\overline{\upsilon'^2_i} \tag{35}$$

For simplicity the K is not written as K', but it is indeed the energy of the fluctuating velocity component of the decomposition. Note that neither the mass nor density are factors in this kinetic energy. In Equation (33), $\mathcal{P}$ is the turbulent kinetic energy production rate term defined as

$$\mathcal{P} = R_{ij} \frac{\partial \overline{\upsilon_i}}{\partial x_j} \tag{36}$$

Assuming that the Boussinesq hypothesis proposed in Equation (21) holds, then Equation (36) becomes

$$\mathcal{P} = \nu_t \frac{\partial \bar{\upsilon}_i}{\partial x_j}\left(\frac{\partial \bar{\upsilon}_i}{\partial x_j} + \frac{\partial \bar{\upsilon}_j}{\partial x_i}\right) \tag{37}$$

Since the K-ϵ model uses a separate closed differential (transport) equation for ϵ, the only remaining term requiring modeling in the K transport equation is the last term. It is traditional to assume the term follows a gradient transport law[22] such as,

$$\frac{1}{\rho}\overline{p\upsilon_i'} + \overline{\upsilon_i'(\upsilon_j'^2/2)} = -\frac{\nu_t}{\sigma_K}\frac{\partial K}{\partial x_i}, \tag{38}$$

where σ_K and σ_ϵ are turbulent Prandtl Numbers. Finally, substituting this closure model into the K transport Equation (33), it reduces to

$$\frac{\partial K}{\partial t} + \bar{\upsilon}_j \frac{\partial K}{\partial x_j} = \mathcal{P} - \epsilon + \frac{\partial}{\partial x_i}\left[\left(\nu + \frac{\nu_t}{\sigma_K}\right)\frac{\partial K}{\partial x_i}\right] \tag{39}$$

The left-hand side represents convection which is balanced by the right-hand side with production, dissipation, and transport. Lastly, the eddy viscosity is defined algebraically by choosing appropriate velocity and length scales such that $\nu_t = \mathcal{U}\mathcal{L}$. Since K provides a measure of the turbulence, it has been pursued as measure of the velocity scale

$$\mathcal{U} \sim \sqrt{K} \tag{40}$$

Single-equation turbulence models such as S-A, must assume a value for the length scale $\mathcal{L}$ as part of a mixing-length assumption. Thus, single-equation models suffer because they may only work in certain classes of flows and may require externally supplied input for the length scale. A length scale is required for the following dimensional analysis relation to calculate the kinetic energy dissipation rate ϵ,

$$\epsilon \sim \frac{K^{3/2}}{\mathcal{L}} \tag{41}$$

However, a model that automatically selects the length scale is desirable, and this is where two-equation models offer a solution. Since the two-equation models use a separate transport equation to determine ϵ, Equation (41) can then be rearranged instead to estimate the length scale,

$$\mathcal{L} \sim \frac{K^{3/2}}{\epsilon} \tag{42}$$

Multiplying Equations (40) and (42) yields Equation (43).

$$\nu_t = \mathcal{U}\mathcal{L} = C_\mu \frac{K^2}{\epsilon} \tag{43}$$

where $C_\mu = 0.09$ is a constant in the standard k-ϵ model. This gives the two-equation models more robustness because the length scale is not required to determine the eddy viscosity. Next, the energy dissipation rate is governed by a differential equation defined in Equation (34). It is modeled with a combination of terms more challenging to model than the K transport equation (39). The ϵ equation comes completely from empiricism and uses arbitrary coefficients acquired during lab experiments, but behaves reasonably well for a wide variety of flows. Some of the terms are combined

$$\epsilon_{ij} = 2\nu \overline{\frac{\partial \upsilon_i}{\partial x_k} \frac{\partial \upsilon_j}{\partial x_k}}, \qquad \epsilon_{ij}^c = 2\nu \overline{\frac{\partial \upsilon_k}{\partial x_i} \frac{\partial \upsilon_k}{\partial x_j}} \tag{44}$$

$$P_\epsilon^1 = -\epsilon_{ij}^c \frac{\partial \bar{\upsilon}_i}{\partial x_j} \tag{45}$$

$$P_\epsilon^2 = -\epsilon_{ij} \frac{\partial \bar{\upsilon}_i}{\partial x_j} \tag{46}$$

$$P_\epsilon^3 = -2\nu \, \overline{\upsilon_k' \frac{\partial \upsilon_i'}{\partial x_j}} \frac{\partial^2 \bar{\upsilon}_i}{\partial x_k \partial x_j} \tag{47}$$

$$P_\epsilon^4 = -2\nu \, \overline{\frac{\partial \upsilon_i'}{\partial x_k} \frac{\partial \upsilon_i'}{\partial x_j} \frac{\partial \upsilon_k'}{\partial x_j}} \tag{48}$$

$$\Pi_\epsilon = -2\nu \frac{\partial}{\partial x_i} \left(\overline{\frac{\partial p}{\partial x_j} \frac{\partial \upsilon_i'}{\partial x_j}} \right) \tag{49}$$

$$T_\epsilon = -\nu \frac{\partial}{\partial x_k} \left(\upsilon_k' \overline{\frac{\partial \upsilon_i'}{\partial x_j} \frac{\partial \upsilon_i'}{\partial x_j}} \right) \tag{50}$$

$$D_\epsilon = \nu \nabla^2 \epsilon \tag{51}$$

$$\Upsilon_\epsilon = 2\nu^2 \overline{\left(\frac{\partial^2 \upsilon_i'}{\partial x_j \partial x_k} \right)} \tag{52}$$

Except for the last diffusion term D_ϵ, all of these equations contain velocity fluctuations (υ') and must be modeled. P_ϵ^3 is not modeled explicitly, but is considered to be contained within one of the other production terms. First, a model for the first two production terms is considered and relies on the formal assumption that the deviatoric parts of ϵ_{ij} and ϵ^c_{ij} are related to the anisotropy of turbulence and results in

$$P^1_\epsilon + P^2_\epsilon = C_{\epsilon 1}\frac{\epsilon}{K}\mathcal{P} \tag{53}$$

The stretching (P^4_ϵ) and dissipation (Υ_ϵ) terms were derived for isotropic and homogeneous turbulence, but are applied to the general case because there are no means yet of determining the effects of anisotropy on the correlations.

$$P^4_\epsilon - \Upsilon_\epsilon = C_{\epsilon 3}R_T^{1/2}\frac{\epsilon^2}{K} - C_{\epsilon 2}\frac{\epsilon^2}{K} \tag{54}$$

where $R_T = K^2/\nu\epsilon$. Traditionally $C_{\epsilon 3} = 0$ is assumed, in which case no contribution to the dissipation rate balance occurs from vortex stretching. Lastly, the transport terms are treated as a gradient law,

$$T_\epsilon + \Pi_\epsilon = \frac{\partial}{\partial x_i}\left(\frac{\nu_t}{\sigma_\epsilon}\frac{\partial \epsilon}{\partial x_i}\right) \tag{55}$$

After substitution of all the models in Equations (53)-(55), Equation (34) transforms into

$$\frac{\partial \epsilon}{\partial t} + \bar{v}_j\frac{\partial \epsilon}{\partial x_j} = C_{\epsilon 1}\frac{\epsilon}{K}\mathcal{P} - C_{\epsilon 2}\frac{\epsilon^2}{K} + \frac{\partial}{\partial x_i}\left(\nu + \frac{\nu_t}{\sigma_\epsilon}\frac{\partial \epsilon}{\partial x_i}\right) \tag{56}$$

Similar to all the differential equations used in the K-ϵ model, the left-hand side represents convection which is balanced by the right-hand side with production, dissipation, and transport model terms. The default constants for all k-ϵ models are [22, p. 316],

$$C_{1\epsilon} = 1.44, \qquad C_{2\epsilon} = 1.92, \qquad C_{\mu} = 0.09, \qquad \sigma_k = 1.0, \qquad \sigma_{\epsilon} = 1.3,$$

C. Realizable k-epsilon

The realizable k-ϵ model was used during the present work for MESH II, and it differs from the standard and RNG k-ϵ models in that C_{μ} is no longer a constant. FLUENT computes this by

$$C_{\mu} = \frac{1}{A_0 + A_s * \frac{KU^*}{\epsilon}} \tag{57}$$

where

$$U^* \equiv \sqrt{S_{ij}S_{ij} + \widetilde{\Omega}_{ij}\widetilde{\Omega}_{ij}} \tag{58}$$

and

$$\widetilde{\Omega}_{ij} = \Omega_{ij} - 2\epsilon_{ijk}\omega_k \tag{59}$$

$$\Omega_{ij} = \overline{\Omega_{ij}} - \epsilon_{ijk}\omega_k \tag{60}$$

Here, ϵ_{ijk} is the Levi-Civita symbol and $\overline{\Omega_{ij}}$ is the mean rate-of-rotation tensor. Note that the $2\epsilon_{ijk}\omega_k$ term is ignored in the calculation of $\widetilde{\Omega}_{ij}$ because it is an extra rotation term that is incompatible for meshes involving rotating reference frames, as in the present work. The model constants A_0 and A_s are

$$A_0 = 4.04, A_s = \sqrt{6} cos\phi$$

where

$$\phi = \frac{1}{3} cos^{-1}(\sqrt{6}W),\ W = \frac{S_{ij}S_{jk}S_{ki}}{\tilde{S}^3},\ \tilde{S} = \sqrt{{S_{ij}}^2}$$

and S_{ij} is the mean rate of strain tensor defined in Equation (22).

V. Additional Models

In addition to the Navier-Stokes, Reynolds averaging, pressure-velocity coupling, and various turbulence models, FLUENT employs extra models when required. For example, wall functions are used when the near-wall grid spacing is poor, or employs energy equations when temperatures or phase must be considered. The present work both required and employed the standard wall functions, enhanced wall functions, energy equations, and species transport modeling. Wall functions were described briefly in the Spalart-Allmaras section (see Equation (30)), but FLUENT uses wall functions whenever the wall adjacent grid size is too large to resolve the viscous sublayer. If the grid is fine enough, the near-wall approach can be used, however, this requires more cells and computational resources. Equation (43) is modified by supplying an additional wall function f_μ so that it transforms into,

$$\nu_t = C_\mu f_\mu \frac{K^2}{\epsilon} \tag{61}$$

This function is supplied to accommodate what is known as "wall blocking effect" and "viscous damping" that occurs very close to the walls. FLUENT uses a different method by employing the log law of the wall,

$$\bar{\upsilon}^* = \frac{1}{\kappa}\ln(Ey^*) \tag{62}$$

Note that this equation is identical to the log law introduced in Equation (30), except that now the variables for velocity and distance are non-dimensionalized in the following manner,

$$\bar{\upsilon}^* \equiv \frac{\bar{\upsilon} C_\mu^{1/4} K^{1/2}}{\tau_w/\rho} \tag{63}$$

$$y^* \equiv \frac{y_n C_\mu^{1/4} K^{1/2}}{\nu} \tag{64}$$

where the state variables correspond to the shortest distance y_n from the wall to the cell centers. For a range of $30 < y^* < 300$, the logarithmic law for mean velocity is valid, but to ensure that the piecewise function covers the entire domain, FLUENT employs it as long as $y^* > 11.225$. When $y^* < 11.225$ the laminar stress-strain relationship is employed instead, and states that

$$\bar{\upsilon}^* = y^* \tag{65}$$

just as in Equation (29). A common alternative measure of non-dimensional length is $y^+ = \frac{y_n \upsilon_\tau}{\nu}$ from Equation (31). Note that y^* and y^+ are comparable when the wall adjacent cell's centroid is placed within the log layer. It's not advisable to have grid spacing such that the y^* or y^+ values fall within the buffer range. Even though FLUENT supplies a relation for the entire domain, $y^+ \approx 30$ is most desirable to ensure accurate predictions.[1]

If however the grid does happen to fall in the buffer range, as in certain walls of the present work, FLUENT offers enhanced wall functions that allow the solution to be solved for meshes that contain regions of $y^+ \approx 1$ and regions where the wall mesh is coarse $y^+ \geq 30$. The enhanced wall functions employ a two-layer approach consisting of viscosity-affected and fully-turbulent regions where they are segregated based on a Reynolds number defined as

$$Re \equiv \frac{\rho y_n \sqrt{K}}{\mu} \tag{66}$$

and MESH II employs this enhanced wall function method to overcome the wide range of y^+ values encountered. Further details on the method go beyond the scope of this work, but cant be found in Ref. 1.

A. Dilute Approximation

FLUENT has the capability to model species transport in fluid chemical mixtures, and this method was employed in the current work to model CO_2 transport through air for MESH II. The equations in this section do not use Einstein summations, but rather are left in vector form (vectors are denoted by underlines). Retaining the equations in vector form allows the i subscript to represent the ith species in the fluid mixture. The species transport method involves using the local mass fractions of each species Y_i, and predicting the solution with a convection-diffusion equation for the ith species (note that this is *not* an Einstein summation),

$$\frac{\partial}{\partial t}(\rho Y_i) + \nabla \cdot (\rho \underline{v} Y_i) = -\nabla \cdot \underline{J}_i + R_i + S_i \tag{67}$$

where R_i is the net rate of production of the ith species by chemical reaction and S_i is the rate of creation from a dispersed phase. Both of those terms are ignored in the present work. $\underline{J}_i$ is the diffusion flux vector of the ith species and it arises because of concentration gradients. The dilute approximation is used by default in FLUENT and for the present work, under which the diffusion flux is defined as

$$\underline{J}_i = -\left(\rho D_{i,m} \nabla Y_i + \frac{\mu_t}{Sc_t} \nabla Y_i\right) \tag{68}$$

where $D_{i,m}$ is the diffusion coefficient for the ith species and Sc_t is the turbulent Schmidt number given by,

$$Sc_t = \frac{\nu_t}{D_t} = 0.7 \tag{69}$$

In turbulent flows the laminar diffusion does not play a very large role because the turbulent mixing plays the dominant role. For N number of species in the fluid, FLUENT will solve $N-1$ equations for the concentrations, then use

$$Y_N = 1 - \sum_{i=1}^{N-1} Y_i \tag{70}$$

to determine the Nth species concentration. To reduce numerical error, the last (Nth) species should be chosen as the one with the lowest concentration, i.e. the listed order of species in FLUENT is important. The present contribution used air as the first species, and CO_2 as the second species because it was never expected to rise much above 4% mass fraction.

B. Energy Equations

As a consequence of using species transport, the energy equations must be enabled in FLUENT to account for changes in enthalpy which can significantly effect the solution. Transport of enthalpy due to species diffusion is defined as

$$\nabla \cdot \left[\sum_{i=1}^{N} h_i \underline{J_i} \right] \tag{71}$$

In particular, this term should not be neglected when the Lewis number (Le) is far from unity, where

$$\mathrm{Le}_i = \frac{k}{\rho c_p D_{i,m}} \tag{72}$$

Next, the enthalpy of each cell volume can be computed by summing the contributions from each of the individual species. Thus, it is useful to determine h_i, the enthalpy of the ith species,

$$h_i = \int_{T_{ref}}^{T} c_{p,i} dT \tag{73}$$

where $T_{ref} = 298.15°K$ and $c_{p,i}$ is the specific heat capacity of the ith species. For incompressible flows, the total enthalpy h is then the summation of the enthalpy's weighted by the concentration Y_i with the addition of energy from the local pressure p,

$$h = \sum_{i=1}^{N} Y_i h_i + \frac{p}{\rho} \tag{74}$$

Lastly, the total energy E consists of the enthalpy and the kinetic energy minus the pressure work, respectively,

$$E = h + \frac{\bar{\upsilon}^2}{2} - \frac{p}{\rho} \tag{75}$$

Note that the pressure work has been subtracted and therefore is not present in E, but the pressure work is reintroduced into the convective acceleration term when modeling the energy transport. When the energy equation is enabled in FLUENT, it introduces one additional differential equation to be solved for the variable E,

$$\frac{\partial}{\partial t}(\rho E) + \nabla \cdot (\underline{\upsilon}(\rho E + p)) = \nabla \cdot \left(k_{eff} \nabla T - \sum_{i=1}^{N} h_i \underline{J}_i + (\overline{\overline{\tau}}_{eff} \cdot \underline{\upsilon}) \right) \tag{76}$$

where $k_{eff} = k + k_t$, is the effective thermal conductivity and k_t is the turbulent thermal conductivity defined based on the turbulent model chosen. In this energy transport equation, the left-hand side represents the typical convection terms balanced with the right-hand side representing energy transfer due to conduction, species diffusion (Equation (71)), and viscous dissipation, respectively. Most often the pressure work p/ρ and kinetic energy $\bar{\upsilon}^2/2$ terms in Equation (75) are negligible in incompressible flows. The present work employs the pressure-based solver, and under these conditions, FLUENT ignores those terms.

VI. Objectives

The present contribution aims to gain an understanding of the flow field in the cavity and interactions between the seal ring and mainstream air, namely the occurrence of ingestion. A better understanding may help to improve future turbine seal ring designs that require little or no purge air. As stated before, the purge air reduces the turbine efficiency by removing compressed inlet air (that could otherwise be used in combustion) to be used instead as coolant flow to the internal components. Many critical components could otherwise be damaged from ingestion of hot mainstream air - namely the rotor disk because it experiences much higher mechanical stresses during operation. Cost savings and weight reduction in materials are also a major motivation in cooling methods. The combined approach of performing experiments and simulations will give some insight on the computer model's capabilities of predicting the flow. If the correlations between experiment and simulation are high enough, one might be able to make some conjectures about the reasonableness of the obtained solution. Simulations already play a crucial role in modern turbine design because they offer the ability to observe the flow in ways that are impossible experimentally.

Experiments yield real data, but the type of data that can be extracted is limited to forms such as pressure at a single point or velocity in a plane. Simulation data can be extracted anywhere within the domain, however, due to the quite large amounts of data, it is still difficult to monitor (let alone compare), for example, instantaneous velocity fields. Fourier analysis becomes useful in unsteady simulations with time-periodic behavior, but as with most other variables of interest, the value must be a single measured quantity such as an average over a volume, surface, curve length, or single point. Comparisons between the simulation results and the experimental measurements are made whenever possible in the present work, but additional comparisons are also made between the two simulations.

A. Historical Approaches

Historically, simulations were more restricted in capabilities due to computational resource limitations. Many of the older more primitive turbine and cavity simulations used simplifying assumptions such as steady-state, 2D axisymmetric in polar coordinates,[27] absence of blades and/or vanes, or boundary conditions lacking a far field characteristic. The current contribution still contains simplifying assumptions (namely the circumferential periodicity), but the increased complexity and sophistication of the model grid allows the problem at hand to be more accurately defined in hopes that the resulting solution will also be more accurate.

The accuracy can be quantified by carrying out an experiment and comparing the measurements obtained to the simulations. Typical measurements of interest for fluid flows include using instrumentation such as pressure taps, concentration taps, thermocouples, and particle image velocimetry (PIV) methods; all of which have been used during the experiments in the present work and many previous works.

B. Scope of Investigation

The present contribution attempts two main goals. First, it attempts to determine whether a simulation in FLUENT can closely predict the flow characteristics measured in an experimental model turbine rig. Secondly, the results from the experiments and simulations are used to help understand what causes ingestion to occur. Two different simulations were performed, and though it is interesting to compare the two simulations (MESH I and II) with one another, that is not the main purpose of the present work. Each simulation was attempting to reproduce the experimental results with the highest accuracy possible. Therefore, to isolate exactly which alterations or upgrades from MESH I to II and how they affect the solution results, cannot be readily determined.

The geometry and boundary conditions supplied to the simulation are made as accurately as possible. Uncertainties in the measurements are described in the Experimental Apparatus section, and the Simulation Methodology section describes the simplifying assumptions made to accommodate a simplified computer model of the actual turbine rig. Results obtained for comparison include pressure and concentration measurements along the stator wall at various radial locations. Additionally, pressure measurements were acquired at the turbine outer shroud at various azimuthal locations. Lastly, PIV plots were obtained to measure radial and tangential velocity components at various axial locations inside the cavity. A subsequent unsteady simulation was performed using MESH II in an attempt to predict ingestion because, as expected, the steady-state model MESH I did not show ingestion after converging.

VII. Simulation Methodology

Experiments were performed on a model turbine rig, with the intent of replicating the experimental measurements with a computer software model. A computer model was developed during the present work using SolidWorks and Gambit, then FLUENT was utilized to process the calculations and perform post-processing analysis. Two different mesh configurations were employed and two unique solutions were generated through the methodology process described below. Compressible effects were neglected for this turbine setup, but it may need to be considered in Mach Number > 1 flows where shock effects may be significant.[16] Presenting the results from a time-dependent model of an unsteady case is difficult. FLUENT was used to produce a majority of the visual representations in this paper, but Tecplot was used to produce time-dependent 3D animations which offered insight on the physical flow features leading to ingestion.

A. Mesh Generation

First, a three-dimensional geometry was created using SolidWorks given initial geometry based on blueprint drawings, and then imported to Gambit with the essential turbine features, i.e. fluid volumes and walls. Gambit was then used to further define face features such as sliding interfaces, boundary inlets/outlets, and periodic faces. In addition to the boundary types, the mesh within the fluid volumes was generated next for subsequent simulation in FLUENT. This is the phase where MESH I and II differ from one another. MESH I was entirely unstructured, which allowed for clustering of cells in important regions, but not providing means to control the quality of the mesh with ease. MESH II employed structured cells in regions ensuring a higher quality grid in delicate regions as described later in this section.

Mesh quality is very critical to the solution stability and accuracy. Node point distribution, smoothness, and skewness[1] are all associated with the quality of the mesh and are described in detail here. Furthermore, the flow field results must generally be known beforehand to produce a suitable mesh spacing. A common issue is determining the first cell height, or wall normal distance y_n directly adjacent to all walls because a proper y^+ value is required and depends primarily on the fluid properties and velocity near the wall. More importantly, if the velocities at the walls are unknown, it is best to maintain a constant mesh spacing along faces where velocity is expected to remain constant. MESH I provided valuable insight on the solution for developing the updated MESH II. FLUENT has some post refinement capabilities, but they are limited to refining the existing mesh. For example, FLUENT is unable to shift nodes on walls, and is also unable to perform smoothing operations once a hanging-node adaptation has been performed. Furthermore, smoothing and swapping may only be performed in a serial case, not in a parallel (multi-CPU) FLUENT case. Smoothing operations are the only method to correct cell skewness because refining will only divide the skewed cell into smaller-volume equally-skewed cells, i.e. the child cells inherent the parent's skewness. Lastly, FLUENT cannot shift nodes on walls or coarsen cells beyond the original mesh; therefore, it is preferable to create the most suitable mesh possible from within Gambit. MESH I lacked quality in some regions and those errors and limitations led to the creation of MESH II in Gambit as described later.

B. Model Assumptions

Computational load requirements were reduced by employing some simplifications to the geometry modeled in the simulation. These simplifications were applied at the very first stage with the 3D SolidWorks model. Therefore, some differences exist between the experimental apparatus and the three-dimensional simulation model. First and foremost, the mesh is only a 1/14th section of the entire turbine configuration and encompasses four blades and four vanes within its rotationally periodic section. While the experimental apparatus has 59 blades, 52 vanes, and 30 purge air injection holes, the CFD model has the *equivalent* of 56 blades, 56 vanes, and 28 purge air injection holes when employing a circumferential periodicity in the simulation. Secondly, the experimental rig has a front cavity and a rear cavity, but only the front cavity is studied in the experiments and the rear cavity is absent from the simulation entirely. Except for these changes, the simulations attempt to mimic the turbine rig geometry exactly based on the detailed drawings. Obviously, as a consequence of the periodicity, gravity effects have been ignored. All of these simplifications were made to reduce the computational domain and thus the computational load.

Though it is commonly accepted that a Mach number greater than 0.3 may

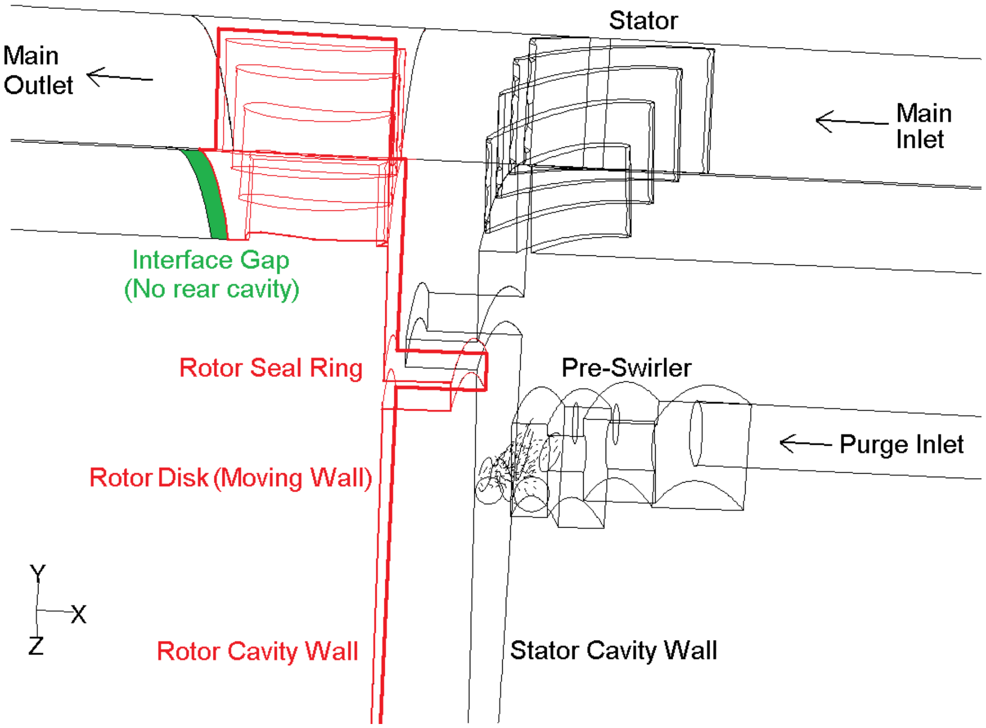

Figure 5. Simulation geometry

begin to show compressible effects, and the MESH II model had a Mach number of about 0.32 at the rotor blade walls, previous simulations have shown general agreement with experimentally measured ingestion using incompressible models.[6] Gentilhomme[16] *et al.*described that the Mach number effects were still weak for Reynolds numbers an order of magnitude larger ($\approx 6 \times 10^6$) and a Mach number (≈ 1). Furthermore, the incompressible model helped reduce the already intensive computational requirements, further substantiating its use in the present work.

C. Boundary Conditions

FLUENT was used to calculate the solution once the mesh was finalized. The procedure involved setting up the boundary conditions at all boundary surfaces and defining wall movement. Both MESH I and II used the same boundary conditions - the rotor wall rotates at 3000rpm about the negative x-axis. Table 2 shows the boundary conditions supplied to the simulations from the matching experimental measurements. Note that the initial pressures supplied are not fixed in FLUENT as they can vary for the type of boundary employed. Thus, the absolute pressure at any point is not important, only the pressure gradients are important. However, FLUENT has the ability to set the (x,y,z) coordinates of a cell that should be used as a reference (zero) pressure to keep the solution values form floating.[1] By default in FLUENT this location is at the origin (0,0,0).

Table 2. Simulation Boundary Conditions for Air

Boundary	Mass Inflow (kg/s)	Initial Gauge Pressure (Pa)	Hydraulic Diameter (m)	Outflow Rate Weighting
Main Inlet	0.080	-1615.5	0.034	
Purge Inlet	0.001113	-3768.2	0.01016	
Main Outlet		-4758.1		0.9973
Purge Outlet		-6309.6		0.0027

1. Mass Flow Rates

The mass-flow rate boundary types were chosen over the pressure boundary types even though both data were available from the experiment. Note that velocity boundaries would behave identically for this incompressible simulation, but would require converting the mass flow rates from the experiments into velocities. Mass flow boundaries offered an easier defining method by requiring only the inlet rates and a mass outflow rate weightings; furthermore, it also ensured that the mass flows would be correct instead of relying on the solver to compute the mass flow given only the pressure boundaries. However, in hindsight, it would have been simpler to employ pressure boundary conditions instead. Firstly, it would have ensured that the absolute pressure values throughout the entire domain were directly comparable with the experiment, and secondly, it would have been useful at the purge outlet where there were two boundary faces, one rotating and one stationary. The mass flow rates had to be estimated for both these purge exit faces individually based on the ratios of their areas.

2. Wall Movement

Depending on the type of simulation (steady or unsteady), the wall movement can behave two slightly different ways. In the present work, the x-axis is defined as the axis of rotation and a rotational velocity is imposed on the rotor wall. Thus all faces adjacent to the moving walls are given a corresponding linear velocity ($\underline{\omega} \times \underline{r}$) and no-slip conditions are present at all the walls. In a steady-state case, as was performed for MESH I, the walls still have a non-zero wall boundary velocity, but the walls do not actually move because no time-advancement iterations occur. This solver method is commonly referred to as a "frozen-rotor" simulation when dealing with turbines, and can be useful for determining aspects of the flow features, but cannot predict unsteady effects that are very critical for ingestion to occur. Most precisely, the steady-state model employs the restriction that $\frac{\partial \upsilon}{\partial t} = 0$, where υ may be a quantity other than velocity such as turbulent eddy viscosity ($\tilde{\nu}$), kinetic energy (K), kinetic energy dissipation rate (ϵ), etc. in the acceleration term of all governing equations.

MESH I was incapable of performing an unsteady case properly due to the grid setup, i.e. lack of ability to incorporate a sliding interface. MESH II was created with sliding interface capabilities and an unsteady case was performed. Unlike the steady-state case, during the unsteady simulation the rotor wall does displace at each time-advancement iteration - known as a "transient-rotor" simulation. To allow for a more accurate solution however, it is often necessary to perform additional iterations within each time-advancement so that the solution may reach convergence before proceeding to the next time step. Note that the $\frac{\partial v}{\partial t} = 0$ is no longer imposed, but is actually calculated based on the current and previous time step (first order method) as well as being used through integration to advance the state-variables through time. In the present work, 35 frozen-rotor iterations were performed between each transient-rotor time-advancement iteration; more details are given in the time step study section.

Additionally, FLUENT gives warnings when a moving and non-moving wall lie adjacent to one another, however, the simulation worked without any problems in both meshes with that type of configuration. Instead of modeling the rear cavity, the interface gap shown in Figure 6 (colored green), acted in place of the rear cavity inlet.

The greatest challenge in modeling moving walls is dealing with the mesh setup. Unlike a simulation that uses a Lagrangian coordinate system to track particle positions that behave as fluids (such as smoothed particle hydrodynamics), the positions

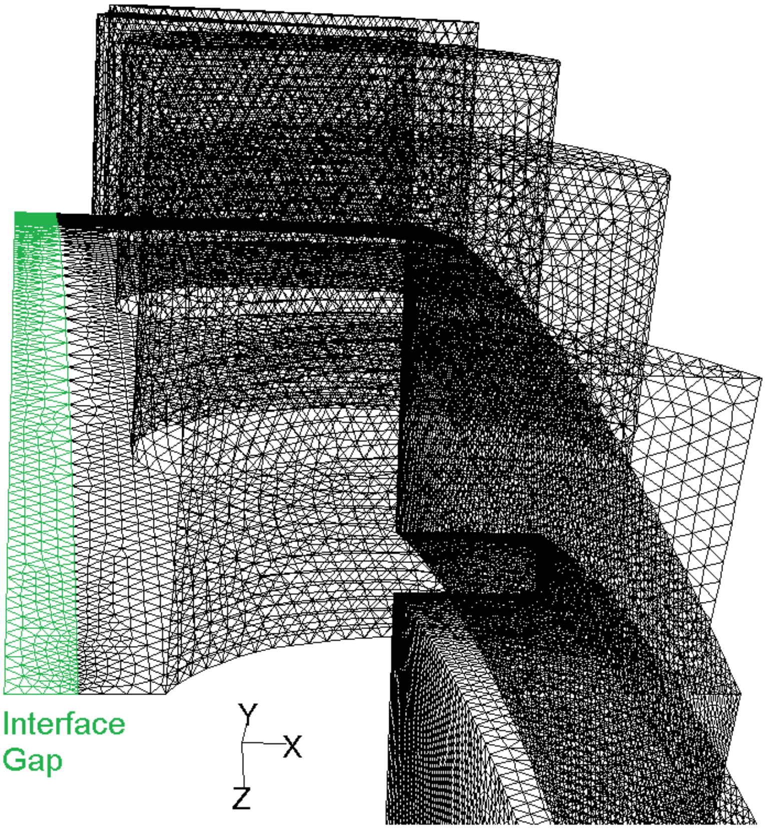

Figure 6. MESH I - Adjacent moving and non-moving walls where rear cavity inlet gap would normally appear

of the fluid properties are fixed to the grid cell locations. Therefore, a moving wall will require the adjacent mesh to move as well. Furthermore, parts of the geometry must remain fixed, such as the main annulus and stator walls. FLUENT offers sliding interfaces as a solution to handle moving walls in transient cases. These interface surfaces act as a communication link between moving and stationary adjacent meshes. This works by having two geometrically identical faces superimposed on one another, one associated with the moving mesh and the other associated with the non-moving mesh. As the two volumes slide past one another, their interface surfaces remain superimposed. Figure 7 shows an example of a 2D sliding interface (a line). The interface works in conjunction with periodic surfaces for a periodic section by creating new periodic zones where the sliding interfaces are no longer superimposed after rotational translation. Note that this requires the periodic sections in MESH II be of the same periodic angle. The same method is applied in 3D

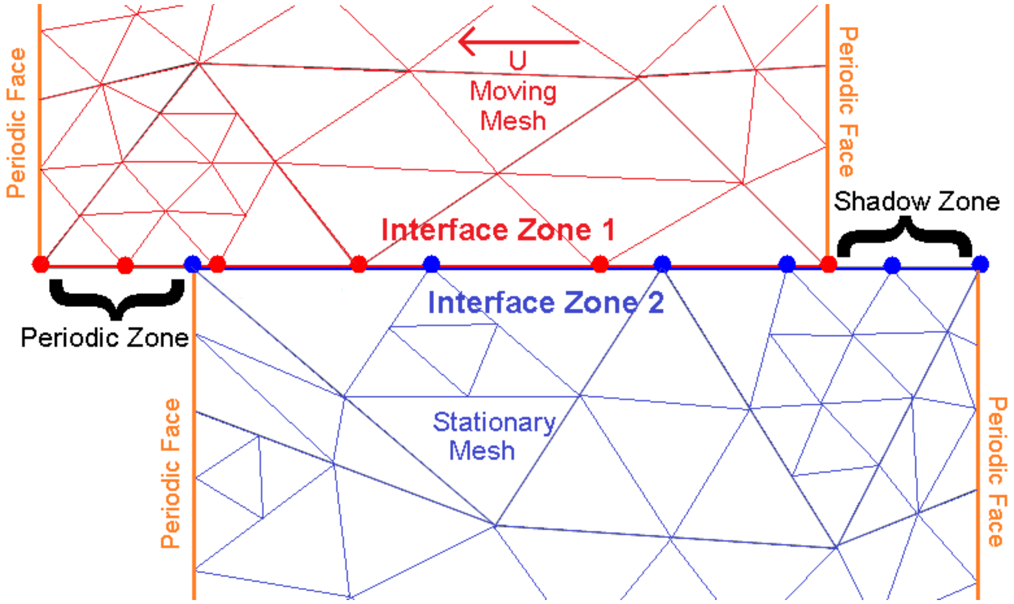

Figure 7. Method used to interpolate sliding interface nodes

for a sliding interface surface. In MESH II, the sliding interfaces in the r-φ plane are flat, but where they lie in the axial-radial plane, they are curved, like a cylindrical surface, making angular rotation possible. Figure 8 shows the sliding interface planes which segregate the moving and non-moving fluid volumes. Sliding interfaces need not have the same face grids because FLUENT creates a new interior zone using nodes from the intersection of both overlapped sliding interfaces (an interior zone, or face, has fluid on both sides). Next, FLUENT can compute fluxes across the two interface surfaces using this interior face, allowing the two fluid zones to *communicate* with one another.

After each time-advancement and rotor displacement, the interior zone must be recreated based on the new node positions of both interfaces. FLUENT also offers the ability to deform meshes with a dynamic mesh, but for MESH II, no mesh deformation is necessary. Rotational mesh motion about the x-axis is sufficient when employing cylindrically shaped volume interfaces. FLUENT also requires that there be "a few" fluid cells between periodic walls so that the sliding interface can properly form an interior face. During tests on MESH II, it was determined that three cells circumferentially across sufficed for FLUENT to run properly, otherwise it would crash the software. More detail is described in the MESH II section.

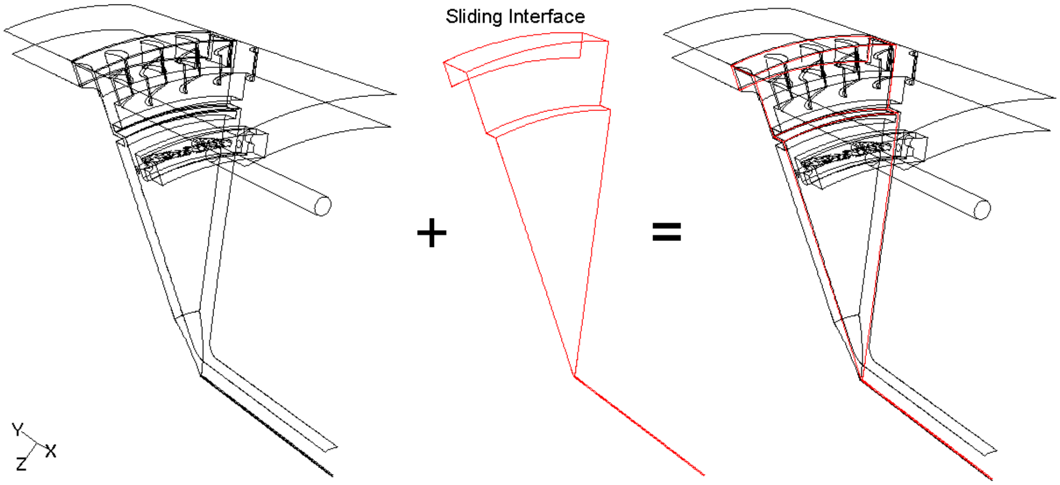

Figure 8. Location of the interface - segregating the moving and non-moving fluid mesh volumes

D. Initial Investigation with MESH I

MESH I consisted entirely of tetrahedral cells in an unstructured grid and was designed to run a steady-state solution only. Once it was determined that the MESH

I grid quality was not performing exceptionally well for the simulation, the primary purpose became to produce a general solution that could be used for designing an updated MESH II. A detailed explanation of the shortcomings will follow in this section.

MESH I calculations began at single precision, first order accuracy with the intent of increasing the accuracy once the solution converged, i.e. periodicity was noticeable between each blade pitch. However, the initial solution required many more iterations than the steady-state MESH II did for convergance, but eventually the accuracy was increased to double-precision and second order accuracy, and the solution produced some useful results.

Initially, MESH I consisted of only two million cells and a coarse grid in most regions. The methodology being to use FLUENT for "solution-adaptive" refinements, by refining regions of high velocity gradient as the solution converged. This was helpful in refining important regions near the blades and vanes. However, it was later determined that the y^+ values at the cavity walls were within the buffer range $4 < y^+ < 30$ and that the those walls would need to be refined. This was first noticeable in the velocity plots that would be used for PIV comparison. The vector field near the stator wall was very erratic and noisy in appearance and a $y^+ \approx 20$ was observed on the stator wall. Upon viewing the cell distribution on the wall as shown in Figure 9, one could see why the y^+ values fluctuated so greatly. The mesh quality needed improvement, especially because the wall contained successive ratios in directions where the cells should have remained a constant size. For example, at a fixed radius in the cavity, it is most desirable to have the same general cell size along the entire circumference. Suppose a cell of volume V can be used to describe the general size of a cell, and can loosely define the mesh's local properties. With that definition, it is desirable to ensure that $\frac{\partial V}{\partial \varphi} = 0$ for a periodic section model, which was clearly not the case in the cavity of MESH I. This hindered the performance of MESH I and led to many successive wall refinements. Furthermore, remnants of the velocity gradients adaptations can be seen near the seal rings in Figure 9 where more turbulent interactions from the pre-swirler are occurring.

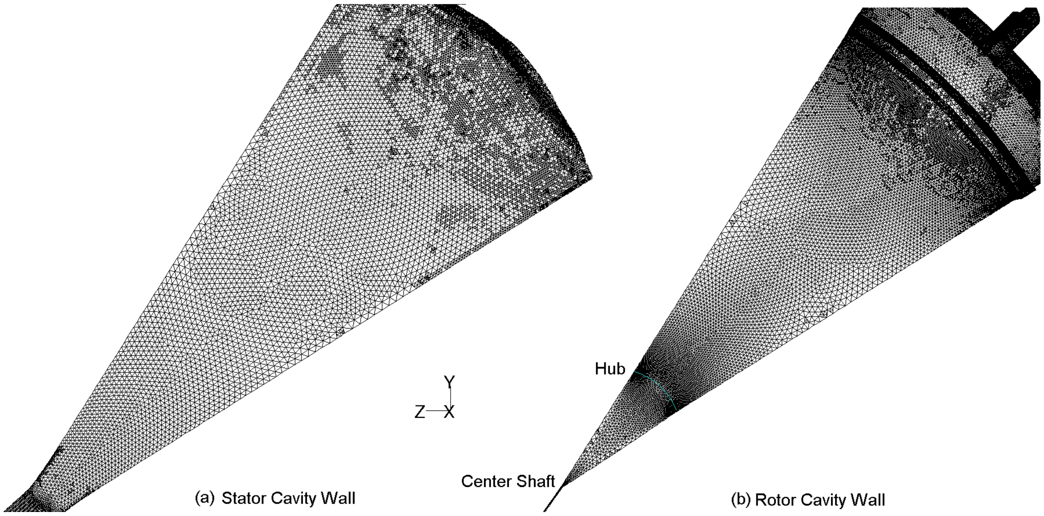

(a) Stator Cavity Wall

(b) Rotor Cavity Wall

Figure 9. Cavity wall showing large variation in cell volumes before any y^+ refinement adaptations

Figure 6 also shows an improper use of successive ratio along the interface gap where the cells become much coarser toward the center (bisection) angle of the periodic section. As a consequence, the solution showed periodic behavior because the cell sizes are inconsistent across the periodic angle. This also made refining the wall difficult because cell volumes can vary significantly (by factors of 8) between neighboring cells that have different refinement levels. Note that y^+ values are directly influenced by the cell size (and thus y_n) and this caused erratic results on the stator cavity wall as depicted in Figure 10. Each line on the graph represents a specific azimuthal angle over the entire 25.7 degree span, and these results indicate a large variation in velocities near the stator wall (x=14.5 mm).

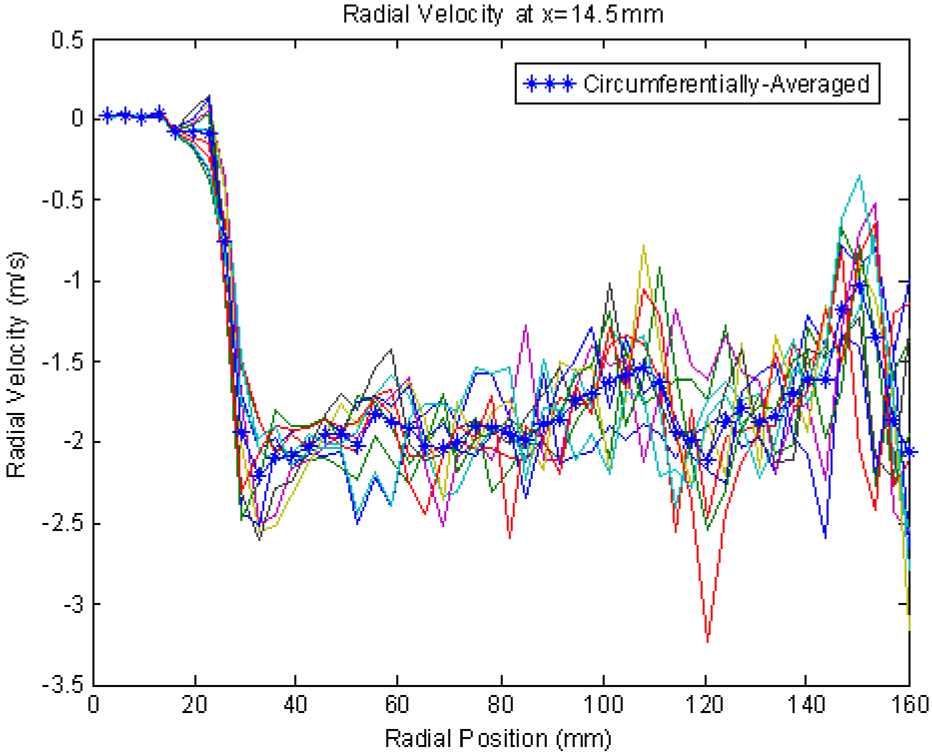

Figure 10. Noisy results near stator wall due to improper y^+ and cell size variations

FLUENT will not coarsen a mesh beyond its original grid, and so increasing $y^+ > 30$ was not an option. The only remaining option was to decrease $y^+ < 3$, which can only be done by refining the cells along the wall. While attempting to do so on the stator cavity wall, the number of cells was increased drastically, by about an additional ten million. This is because the tetrahedral cells adjacent to the wall were being divided into smaller cells. A single cell becomes eight cells during each refinement, while each new cell has about half the width of the original. This is accomplished by trimming each corner of the tetrahedral cell, and introducing the shortest diagonal to the remaining inner octahedral that forms 4 new tetrahedral cells.

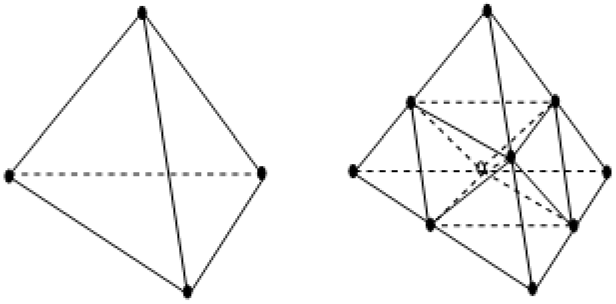

Figure 11. Refining a tetrahedral cell[1]

As a consequence, the cell count at the wall increases by a factor of eight, but the y^+ is only reduced by about a factor of two. As such, after each refinement, only the wall adjacent cells are further refined, and this produces a logarithmic "successive ratio" perpendicular to the wall. The new cell length at the wall is on the order of $\frac{1}{2^n}$ times smaller than the original cell length, where n is the number (or "level") of refinements performed on the original cell. Figure 12 shows one of the four adaptations performed to refine the stator cavity wall such that $y^+ < 3$ was achieved. In this single refinement operation alone (v47 to v48), the cell count increased from 7 to 8.6 million cells.

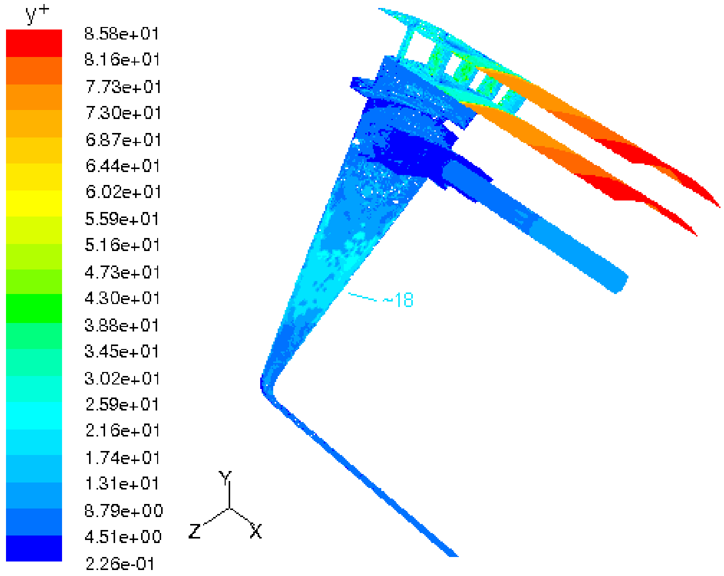

(a) Before refinement (v47)

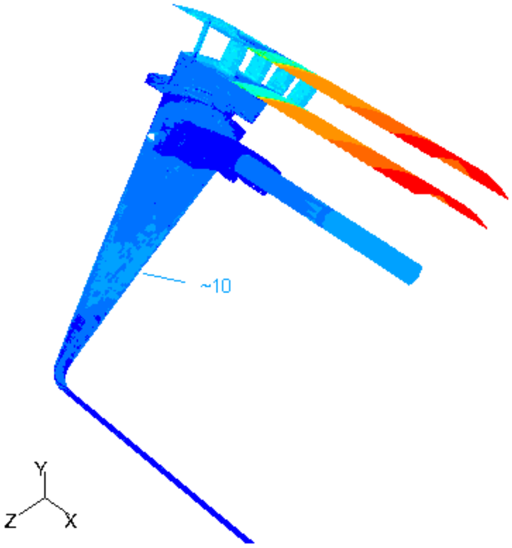

(b) After refinement (v48)

Figure 12. MESH I - Single $y^+ > 3$ refinement effect

Refinements were repeated numerous times until $y^+ < 3$ was achieved at the stator wall, and the logarithmic successive ratio produced perpendicularly to the

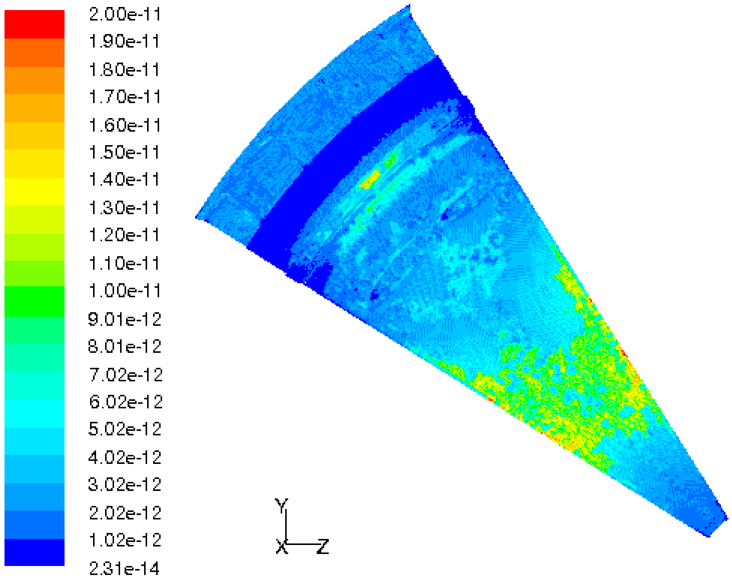

Figure 13. MESH I - Cell volume [m^3] after performing refinement (v48)

wall can be seen in Figure 14. Unfortunately, the computing resources were limited and during the same procedure for the rotor cavity wall, a total of 25 million cells was reached before the $y^+ < 3$ could be achieved. With 25 million cells, the RAM usage became very large, and insufficient CPU resources were available to reach convergence in a timely manner. Table 3 lists some significant refinements that were made to the mesh and the resulting number of cells at each level.

Table 3. MESH I Adaptation History

Adaptation #	Type	Cells
0		2045030
1	Vel. Gradient	3710223
2	Vel. Gradient	4562396
6	Vel. Gradient	6241191
11	Vel. Gradient	6246170
15	Vel. Gradient	6267597
21	$y^+ < 3$ Stator Wall	21240116
25	$y^+ < 4$ Rotor Wall	25585436

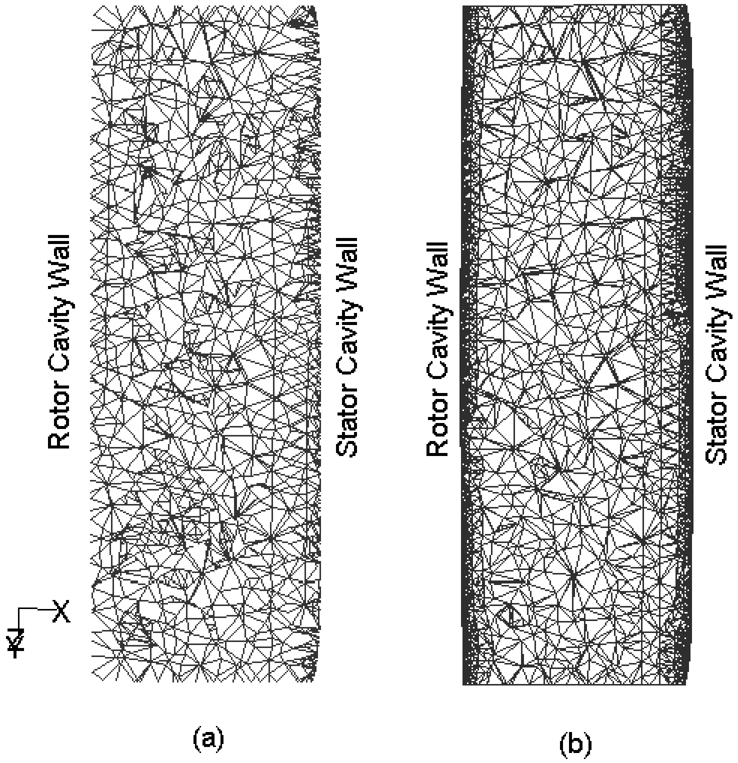

Figure 14. MESH I - Unstructured grid in cavity displaying logarithmic behavior at r=110 mm near wall a) Before and b) After multiple refinements

In conclusion, MESH I successfully tested the limits of the computing power available at the time so that MESH II could be designed with a proper cell count, not to exceed approximately 21 million, where 9 million would be ideal and agile. FLUENT's memory requirements for modeling the finalized steady case of MESH I were over 36GB of RAM and exceeded the computer capabilities. As a consequence, running 1 Intel Xeon CPU required 2 minutes per iteration, and 6 hours were required for all residuals to converge around 1e-5. The residuals would not decrease any lower than this most likely due to the presence of highly skewed cells in MESH I. Lastly, the use of enhanced wall functions may have proven useful and were employed in MESH II as a result.

1. Skewed Cells

Another attempt to improve the solution accuracy was made by trying higher order solver models. This is where MESH I began to encounter issues that could not be overcome within FLUENT. Equiangle skew is the measure of a cells skewness where the ideal value of 0 corresponds to an isometric triangle or rectangular face of a tetrahedral or hexahedral volume respectively. Conversely, a value of 1 corresponds to a completely degenerate cell consisting of coplanar nodes. Skewness is very undesired because gradient evaluations become distorted and often lead to solution divergence. MESH I contained cells of very high skewness (greater than 0.97) at the trailing edge of the rotor blades, and this indeed caused the solution to diverge. As mentioned before, refining the skewed cells does not resolve the issue because the newly created cells inherit the same skewness. This is noticeable in Figure 15 where the skewed cells near the blade trailing edge have been refined. It is also shown in Figure 16 where a few cells with very high velocities (larger than anywhere else in the domain by nearly an order of magnitude) are refined and inherent the same high velocities and skewness.

Inevitably the velocity values in these cells jumped very high when employing higher order spatial accuracy, pressure-velocity coupling models, or under-relaxation factors. Without decreasing the under-relaxation factors from their default values, the MESH I solution would diverge very quickly. Instabilities in the

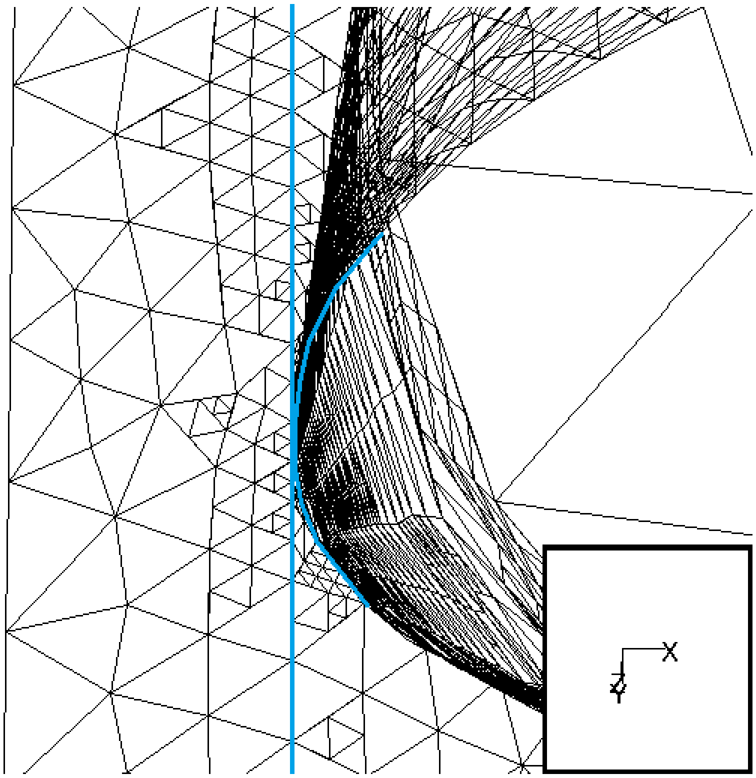

Figure 15. MESH I - Skewed cells at blade trailing edge

solution can be damped out by decreasing under-relaxation factors, but then the solution would take longer to converge.

The only way to correct skewness from within FLUENT was with a smoothing and swapping procedure, and it was less effective near walls because wall nodes cannot be moved. Furthermore, once the hanging-node adaptation method had been performed on a mesh, the smoothing procedure could no longer be employed, thus a new and improved MESH II was needed. Nonetheless, much useful insight came from the MESH I simulation.

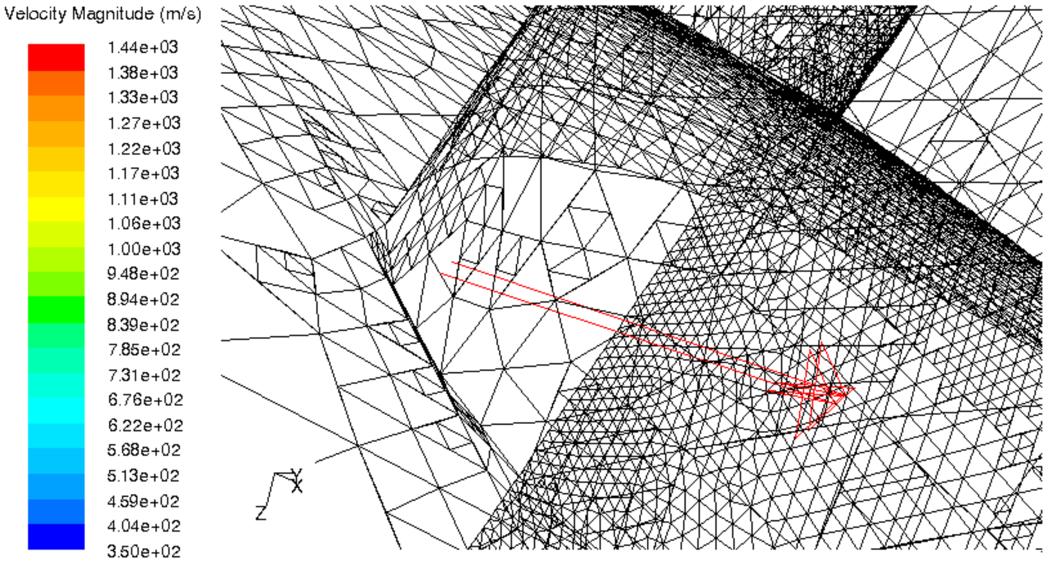

(a) Before

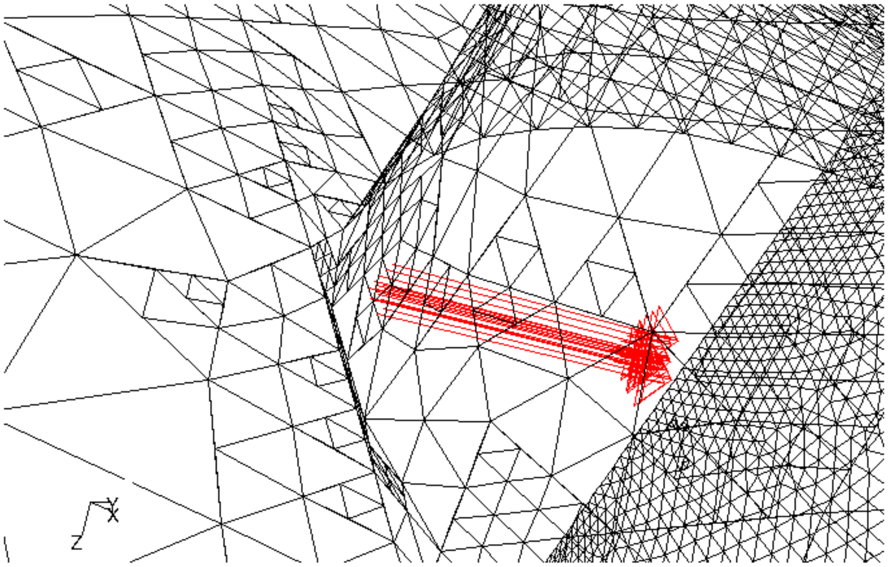

(b) After single refinement

Figure 16. Exploded velocities from skewed cells at blade trailing edge

E. Simulation of MESH II

MESH II had major grid quality improvements, but most notable was the incorporation of a sliding interface to accommodate an unsteady time-dependent simulation. As described previously, utilizing a sliding interface method allows the mesh configuration to displace as the turbine rotates, but requires careful segregation of moving and non-moving mesh portions.

1. MESH II Quality

The intent of redesigning a new mesh was partially to produce a grid containing a reduced number of cells, no more than nine million, and without the need for refinements in FLUENT. This was accomplished by introducing more cells in focus regions such as the seal gap, cavity, and blade/vane interaction region. The cavity was given cells of constant size throughout with an unstructured grid to correct the improper successive ratios by enforcing that $\frac{\partial V}{\partial \varphi} = 0$ whenever possible in the entire mesh. Figure 17 shows the MESH II cavity walls, with a $\frac{\partial V}{\partial r} \leq 0$ to account for higher tangential velocities at larger radii.

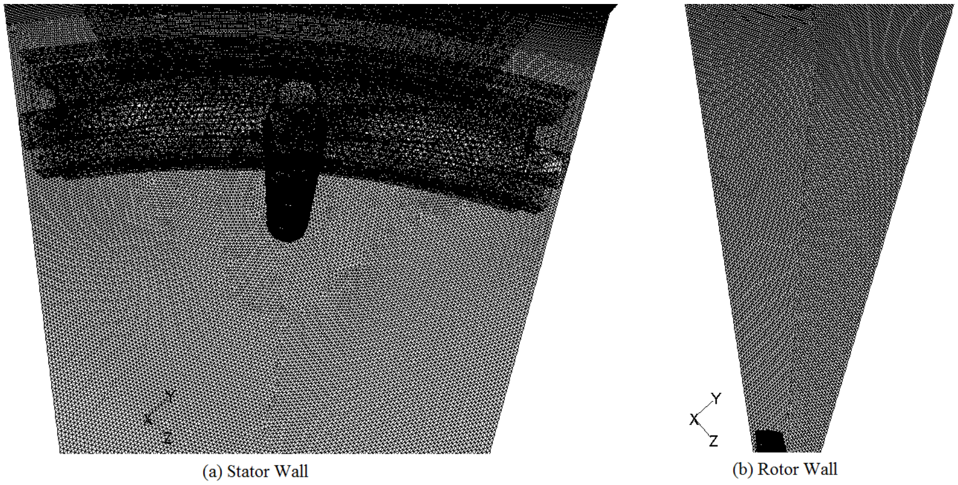

(a) Stator Wall
(b) Rotor Wall

Figure 17. MESH II - Smaller variation in cell volumes along cavity walls

The seal gap was given a much higher cell count and employed a structured grid of hexagonal cells in a cylindrical coordinate system. Taking advantage of the fact that a structured mesh gives more control over the grid quality, the seal radial clearance was designed with 40 cells radially across, and 400 cells along the circumference. These were chosen based on the results of Roy *et al.*[13] where the radial clearance had 20 cells across and 110 cells circumferentially for a 1/25 turbine section. In comparison, MESH II is twice as refined circumferentially while also covering more than twice the circumferential angle. Nearly one million cells alone (out of the total 10 million) were used to mesh the seal gap as shown in Figure 18(a). The results of this very fine mesh region are described later.

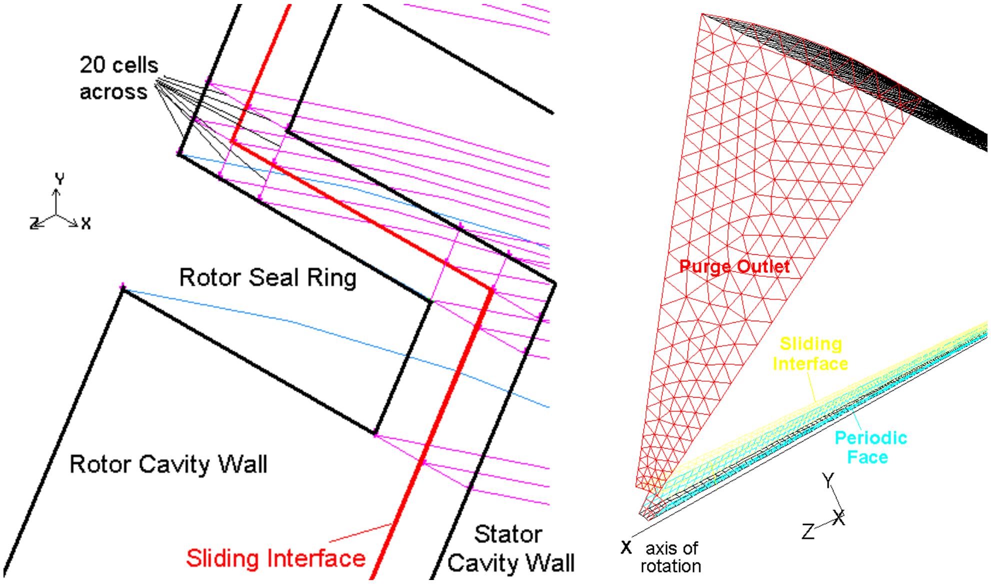

(a) MESH II - Very fine structured seal gap mesh

(b) MESH II - Structured cells along axis near hub purge flow exit

Figure 18. Mesh II structure

Secondly, the clearance gap between the rotor blades and outer shroud was converted into a structured grid. Again, the structured grid was employed because it allowed for more precise control over the cell spacings across the entire outer shroud area. It is essential that there be at least a few cells radially across the gap because the sliding interface passes between this narrow radial gap. A structured grid ensured there be more than three cells radially between the moving and non-moving walls. Figure 19 shows the location of this narrow radial gap.

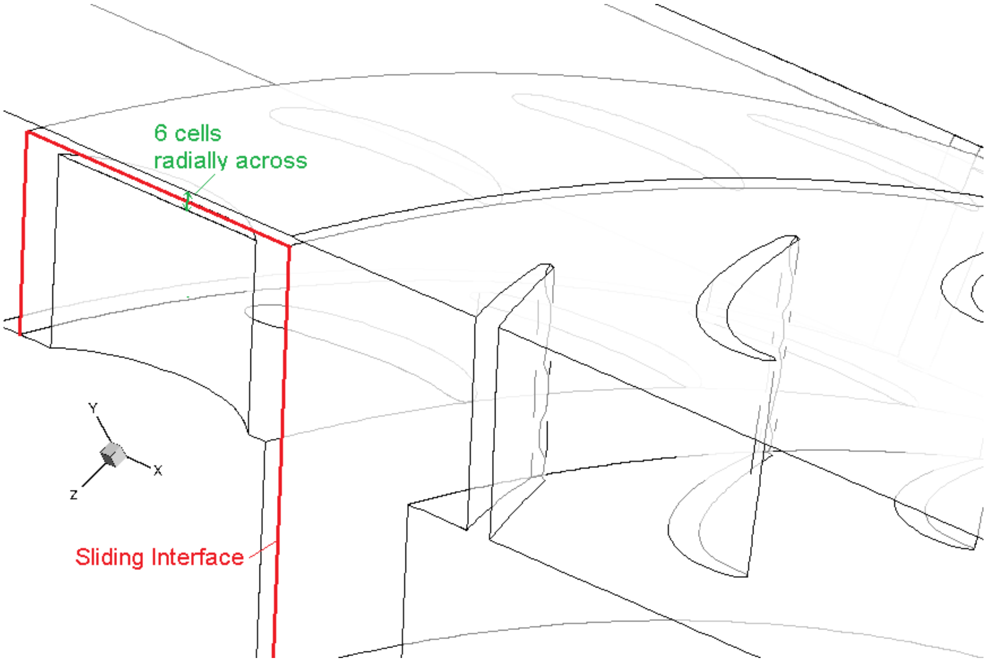

Figure 19. MESH II - Structured grid used in radial gap between outer shroud and blade tops

Furthermore, the same method was employed along the central rotation axis between the purge outlet and rotor hub. In fact, FLUENT would crash when the simulation was attempted and after weeks of extensive searching, it was finally discovered that a lack of cells circumferentially between the periodic faces was causing the sliding interface method to fail. The region initially used an unstructured grid in this narrow region, so upgrading to a hexagonal structured method guaranteed that there would be enough cells circumferentially across the periodic section to create a proper interior face as shown in Figure 18(b).

Lastly, the main annulus was also given a cylindrical coordinate structure, but the cavity, pre-swirler, and regions surrounding the blades/vanes continue to use unstructured meshes because of their complex geometries. In general, structured grids should be used whenever possible to reduce calculation round-off errors.[1]

2. *Skewed Cells*

Next, skewed cells were addressed and corrected. It was realized that since the gap immediately downstream of the rotor trailing edge was being modeled as a wall, the flush edge leading into the cavity was not even necessary, and so the two adjacent faces were merged into one as shown in Figure 20.

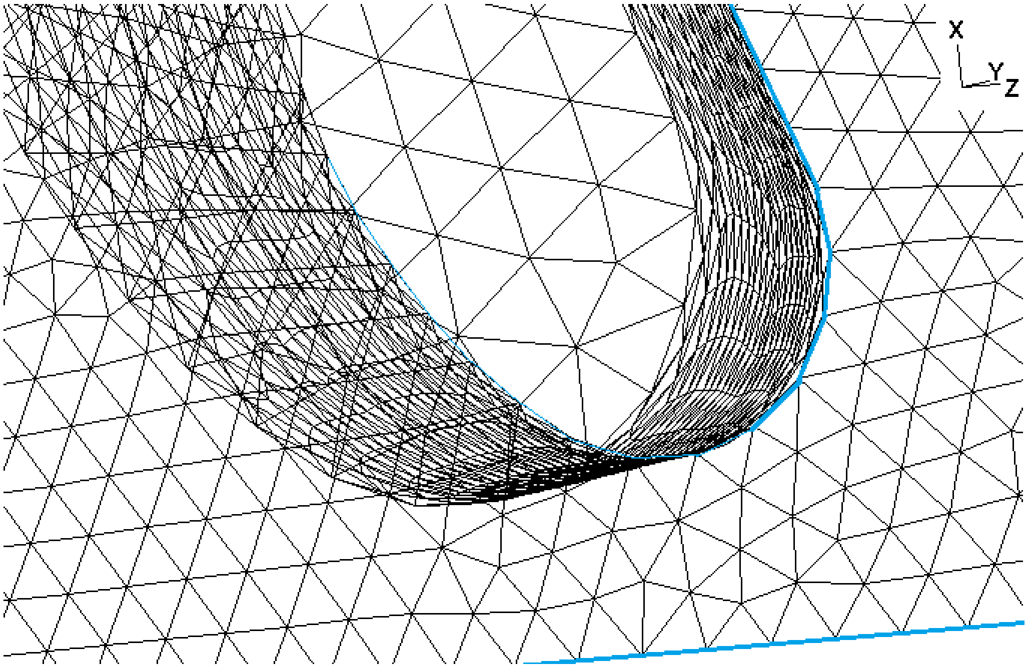

Figure 20. MESH II - Flush edge at rotor blade trailing edge removed by merging faces

This completely solved the skewed cell problem at the blade trailing edge, however, the blade leading edge and vane trailing edge still suffered from the same flush edge problem. The geometry of the turbine dictates that the airfoils be flush with the end-wall edges, but it may be very useful in future projects to leave a small gap for easier meshing. The eventual solution to this dilemma was to keep the mesh coarser, and align the nodes appropriately as to minimize the skewness of any cells as shown in Figure 21.

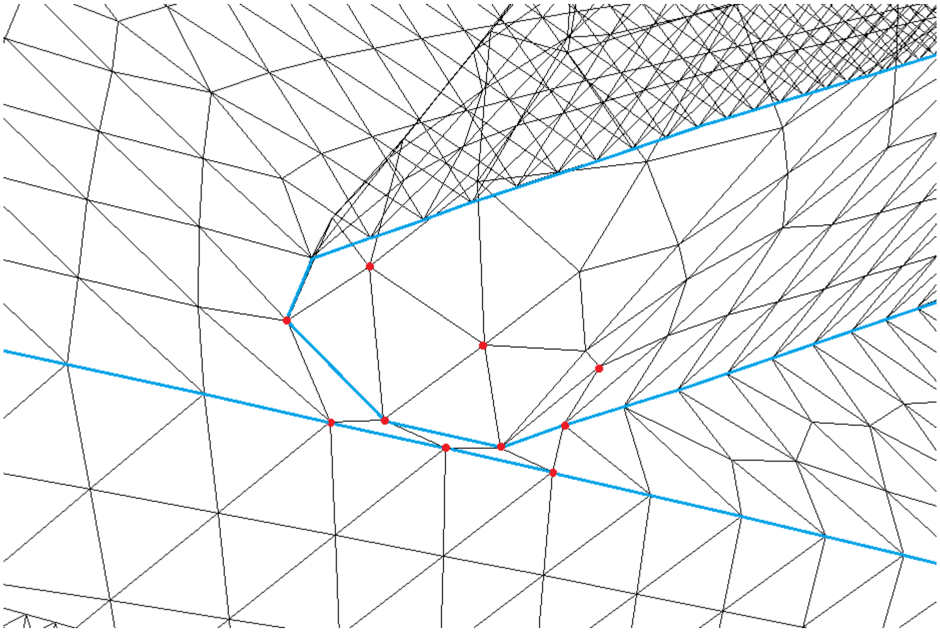

Figure 21. MESH II - Flush edge at vane trailing edge. Skewness minimized with offset node alignment

Even after using Gambit to reduce cell skewness, some cells were still above 0.9 skewness so FLUENT's smoothing/swapping capabilities were employed before running the simulation. The method known as Laplacian smoothing, repositions nodes based on average positions of the surrounding nodes, and can repair severely skewed cells, but simultaneously relaxes the clustering of nodes and may increase the average cell skewness. It should be noted that the operation could only be performed about four times before negative cell volumes appeared. This implies that certain fluid nodes were moving past wall boundaries when smoothed. Figure 22 shows an example of how a negative volume can appear during a smoothing operation. After this procedure the highest equiangle skew did not exceed 0.8 and no convergence issues ever reoccurred after this point.

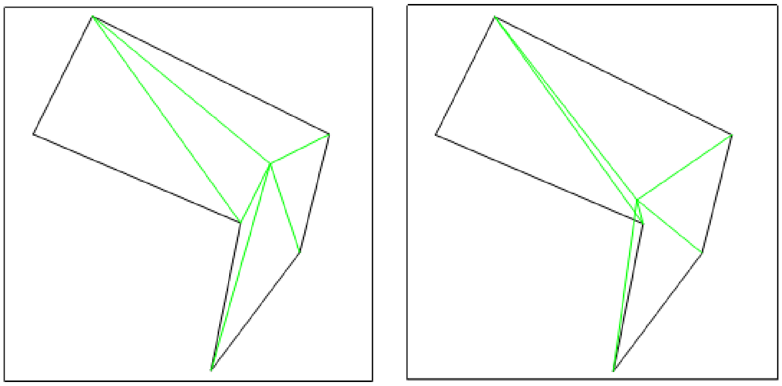
(a) Before smoothing (b) After smoothing

Figure 22. Example of negative volumes being created[1]

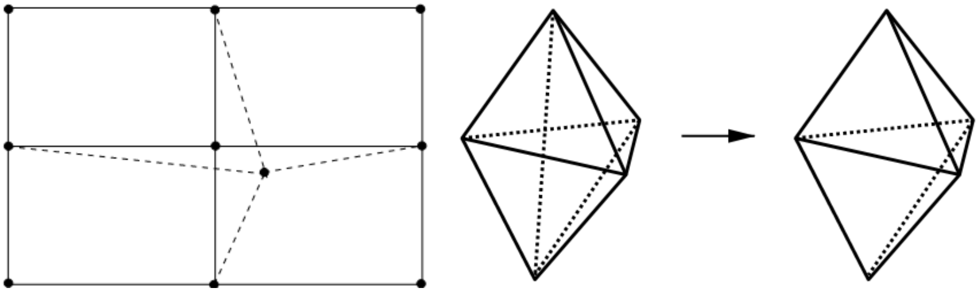
(a) Laplace smoothing example. Dotted line indicated node position before smoothing[1]

(b) Face Swapping example[1]

Figure 23. Smoothing and swapping methods

In addition to smoothing, face swapping was also performed. Face swapping only applies to tetrahedral cells (in 3D), but the algorithm attempts to find at least three cells sharing a single edge that can be replaced by two cells sharing a face. This method simultaneously reduces the cell count while improving the skewness.[1] The overall smooth/swap procedure consists of performing the smooth operation four times, then swapping until no more faces can be swapped, then repeating that process until all skewness decreases below 0.8, but without creating negative cell volumes.[1] To summarize, Figure 24 and Table 4 depict the cell clustering and distribution throughout the mesh.

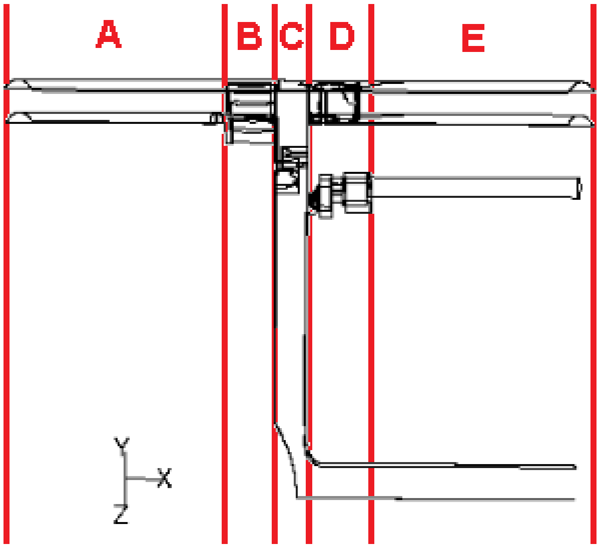

Figure 24. Cell clustering and distribution throughout the mesh

Table 4. Cell Clustering By Axial Domain

Region	A	B	C	D	E
Axial Min. [m]	-0.15	-.03	0	.0165	0.05
Axial Max. [m]	-0.03	0	.0165	0.05	0.15
Contains	Annulus Exit	Blades	Cavity	Vanes/Nozzles	Inlets
Cell Count	155k	451k	7899k	604k	378k

F. FLUENT Simulation

Because the modeling process is ongoing (solution-adaptive), this section describes some preliminary results that were obtained, and used to guide the adaptation in hopes of improving the results further. After having decreased the cell count and skewness as compared to MESH I, higher order models were employed with MESH II. This included the additional use of energy equations which are required for the CO_2 tracer gas transport modeling. MESH I did not use the energy equations and did not model any tracer gas, but for MESH II, the constant dilute approximation was used for mass diffusivity and the mixing law for specific heat. Utilizing the CO_2 transport modeling as a measure of mixing between indigenous cavity air and mainstream air in the simulation presents a directly comparable result to the experiment. Table 5 shows the major differences between the solver settings of MESH I and II.

Table 5. Simulation Characteristics

Mesh	I	II
Incompressible Solver	Steady	Unsteady
Turbulence Model	Spalart-Allmaras	Realizable k-ϵ
Spatial Accuracy	2nd order	2nd order
Final Cell Count	21 million	10 million
Species Transport	None	Air-CO_2 Mixture
Energy Equation	No	Yes
Pressure-Velocity Coupling	SIMPLE	PISO
Gradient Spatial Discretization	Green-Gauss node based	

Instead of the S-A model, the realizable k-ϵ model was employed in MESH II. Also, the pressure-velocity coupling was changed to PISO algorithm because it was highly recommended for transient flows, specifically with large time steps. It increases the time per iteration, but it can drastically reduce the number of iterations required to converge.[1] Figure 25 shows that the solution fluctuates less with the PISO model employed, where the pressure is integrated over the 2D inlet surface to present the mean force acting on the inlet surface.

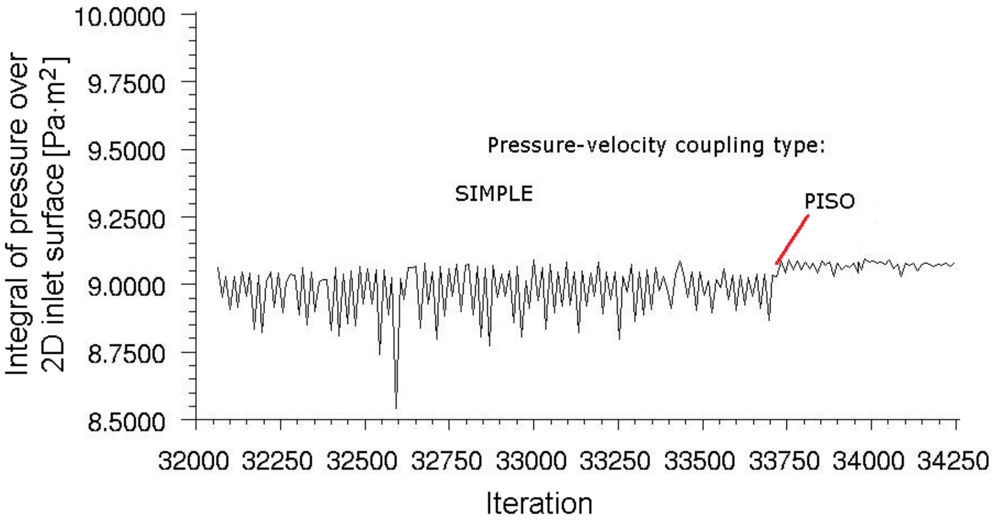

Figure 25. Pressure at main inlet fluctuates less with PISO model

Before starting the simulation of the unsteady flow with MESH II, the steady-state formulation was performed first, and once it converged, that solution became the initial conditions for the unsteady procedure that followed. Furthermore, the simulation began with second order spatial accuracy and double precision, and converged fairly quickly. FLUENT has the option to perform iterations between time steps to improve convergence for unsteady cases. At the beginning of each new time step the rotor-wall rotation and position are updated, and then the solution is iterated within a single time step. Figure 26 shows the residuals during this unsteady case and how the residuals are allowed to re-converge after each time-advancement.

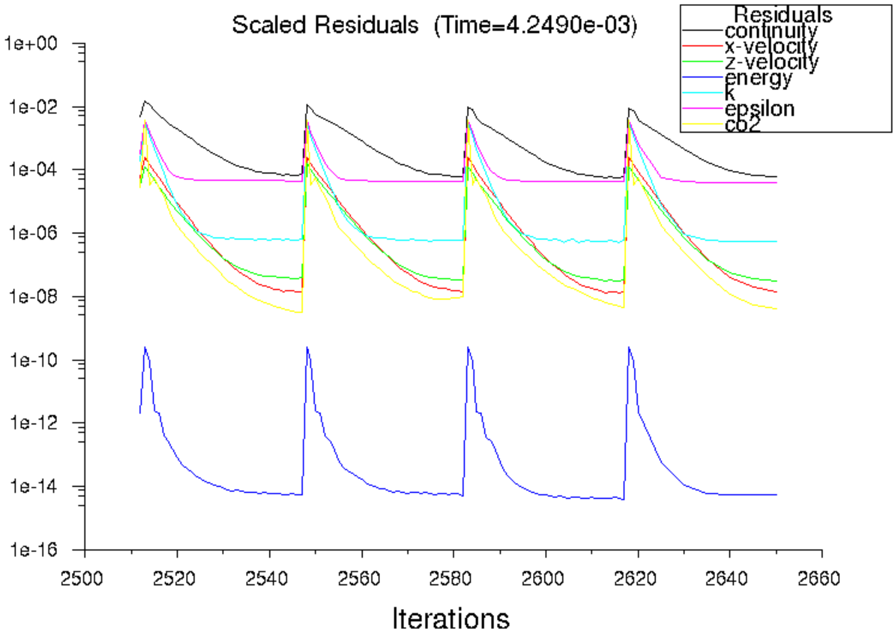

Figure 26. MESH II - Unsteady residuals converging

The calculated instantaneous solutions are accumulated in a growing average, and this statistical mean data is used for comparison with the experimental measurements.

1. Time Step Study

The time step size of Δt =1.75e-6[s] was initially used in the unsteady simulation which allowed 204 time steps between each blade/vane passing at 3000rpm. This was chosen based on a previous unsteady experiment that used 160 time steps per blade passing[13] and had successfully shown that ingestion occurred. Initially during the present simulation, 20 iterations per time-step were used and the residuals decreased to 1e-6, but upon receiving peer reviewer feedback, the iterations per time step were increased to 35 to allow most scaled residuals to decrease sufficiently well below 1e-7 as suggested by the peer reviewer. This also allowed the residuals to level off and stop decreasing before advancing to the next time step, i.e. convergence was reached. The energy residuals were always much lower than any of the others while the continuity residuals were always the highest. Figure 26 shows typical values for the unsteady MESH II case.

Using a small enough time step allows higher frequency disturbances to be resolved, but is not necessarily required to model the major unsteady flow features as was done in a simulation by Montomoli *et al.*[28] Montomoli mentioned that at the current stage of computing power, resolving the Von Karman vortex street in an unsteady case for a complex 3D turbine model is “prohibitive”. Only by reducing the temporal accuracy to filter out the higher frequency responses will the simulation run in a timely manner.

With a Δt =1.75e-6[s] in the present work, the calculation rate of the simulation was 570KHz. This calculation rate was also the “sampling rate” of the produced data. Therefore, in an attempt to deduce if the high rate was necessary, a comparison with experimental FFT data was undertaken. Roy *et al.*[2] performed experiments at two different rpm values for a nearly identical turbine configuration measuring static pressure at the outer shroud. Thereupon, it was determined that the fundamental static pressure frequency is given by the blade passing frequency, and the higher harmonics decline in magnitude as shown in Figure 27 a and b. This suggests that the time step size chosen is more than adequate for producing the most

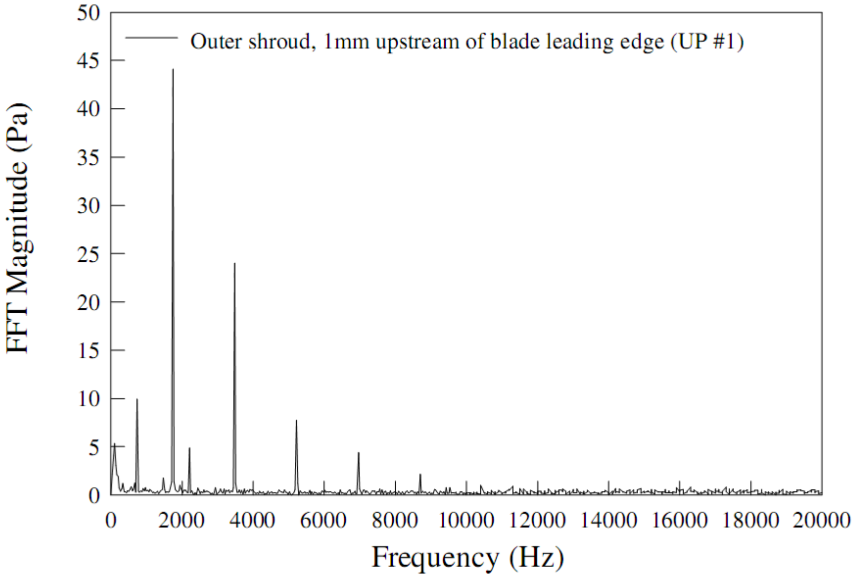

(a) 2000rpm ≈ 1733Hz blade passing

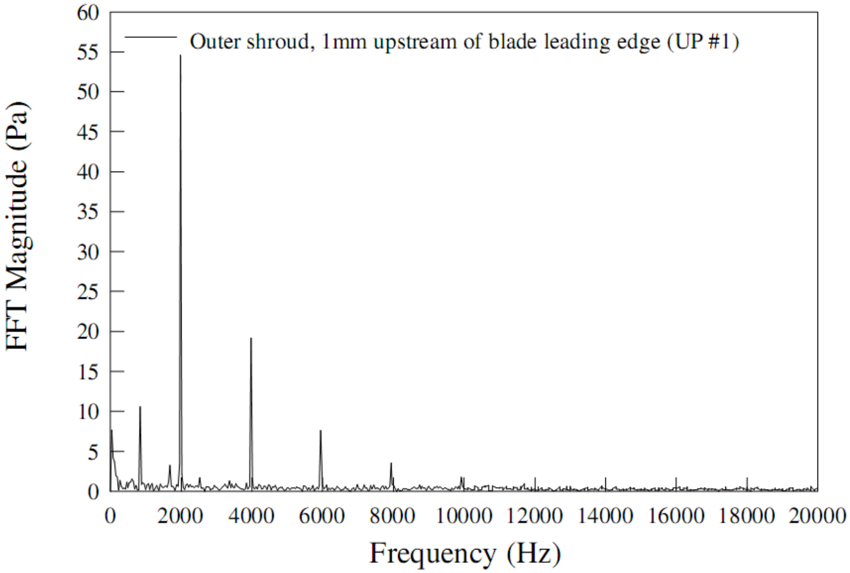

(b) 2290rpm ≈ 2000Hz blade passing

Figure 27. FFT of static pressure 1mm upstream of blade leading edge for nearly identical turbine geometry[2]

significant unsteady disturbances. For the present work, a rotor speed of 3000rpm and 52 blades yields a fundamental frequency of

$$F_0 = \frac{\Omega}{60} n = \frac{3000}{60} 52 = 2.60[KHz] \tag{77}$$

where n is the number of blades on the disk. So for example, by reducing the calculation rate by a factor of five (decreasing the temporal resolution to 41 time steps per blade passing) yields a sampling rate of 114KHz, capable of resolving frequencies up to $F_{max} = 28.6$KHz when generously accounting for aliasing, such that $F_{max} = \frac{1}{4\Delta t}$. Thus, harmonics up to $F_{max}/F_0 = 11$ are capable of being resolved, i.e. the 11th harmonic F_{11} should be realizable and more than sufficient. Whether or not pressure variations of these frequencies will be produced based on this time step size, however, is not guaranteed. In fact, FLUENT did not converge using this larger time step size. The simulation could not remain converged with Δt as large as 5.25e-6[s], or 63 time steps per blade passing (42 iterations per time step). Therefore, efforts to speed up the calculation process by increasing Δt showed that the 200 time steps per blade passing was adequate. Note that modifying Δt won't have a directly proportional effect on the calculation speed because as a consequence, the number of iterations per time step required for convergence will also vary. In summation, the limiting factor on the maximum time step size is actually the solver's ability to converge.

First-order accuracy was employed for the temporal discretization in MESH II. Memory requirements increased significantly when using second order time discretization because FLUENT must store the previous *two* iterations of data instead of just one when computing time derivatives. FLUENT's memory requirements for modeling the unsteady case of MESH II were up to 23GB of RAM. Running 8 Intel Xeon CPU's in parallel required 50 seconds per iteration, for a total of 29 minutes per time step, and 97 hours to compute one blade pitch passing angle. Using a similar grid size with a LES turbulence model is not yet practical for engineering purposes. The computing resources required would be quite large, justifying the choice of the S-A and k-e models. Table 6 shows the comparison between the number of CPU's utilized vs. memory requirements and calculation speed.

Table 6. MESH II Resource Requirements

Number of CPU's	4	5	8
Memory Usage Range [GB]	16-21	17-23	20-24
Time per iteration [s]	70	64	40

2. *Under-Relaxation Factors*

Under-relaxation factors offer a method of dampening unstable solutions so that they may converge, but at the cost of requiring more iterations. The factors are given values between zero and unity, which act as coefficients that determine how much effect the new solution will have on changing the previous iteration's solution. During the simulation, the under-relaxation factors are recommended to start below the default values, then be increased slowly once determined that the solution is stable enough to converge.

With MESH II, the pressure and momentum under-relaxation factors could be

Table 7. Under-Relaxation Factors

Type	Default	MESH I	MESH II
Pressure	0.3	0.3	0.5
Density	1	1	1
Body Forces	1	1	1
Momentum	0.7	0.5	0.7
Turbulent Kinetic Energy	0.8	-	0.8
Turbulent Dissipation Rate	0.8	-	0.8
Turbulent Viscosity	1	1	1
Modified Turbulent Viscosity	0.8	0.8	-
CO_2	1	-	1
Energy	1	-	1

maintained higher than in MESH I and still achieved convergence. The skewed cells in MESH I were likely the main cause of the convergence instabilities that didn't allow the solution to converge less than 1e-5. Increasing these factors any larger than the values shown in Table 7 caused the MESH I solution to "explode".

VIII. Results

Direct comparisons have been made between results of the experiment and the two simulations. All of the instantaneous data in the unsteady MESH II are obtained at exactly the same alignment of blades and vanes as depicted in Figure 8. The mean data for MESH II is ensemble averaged over the entire time domain. Experimentally obtained velocity plots, pressures, and CO_2 concentrations are compared against the equivalent plots extracted from the CFD data. Results here offer valuable insight as to how well the simulation performed.

A. Velocity Maps

PIV images were captured inside the cavity, which spans axially from x=0.0 mm (rotor disk wall) to x=16.5 mm (stator wall). Note that the simulation plots in the r-φ plane are periodically repeated; the 25.71 degree periodicity is noticeable in these plots and no larger flow structures are realizable. Figure 29 displays the edges of the mesh's 25.71 degree periodic boundaries as red lines. Three axial locations within the cavity (x=14.5, 10.2, and 7.1 mm) were measured during the experiment and comparisons are made against simulated velocity magnitude contour maps. The experimental results in Figure 28(a-c) are the baseline for comparison against the two simulations and show the experimental results that were obtained by an arithmetic ensemble-average of ten instantaneous velocity maps. These plots can be compared directly to the MESH I steady simulation in Figure 29(a-c), and the mean and instantaneous results of MESH II in Figures 30(a-c) and 31(a-c).

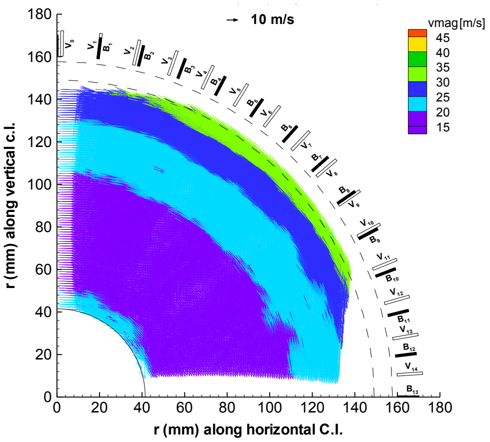

(a) $x = 14.5$ mm

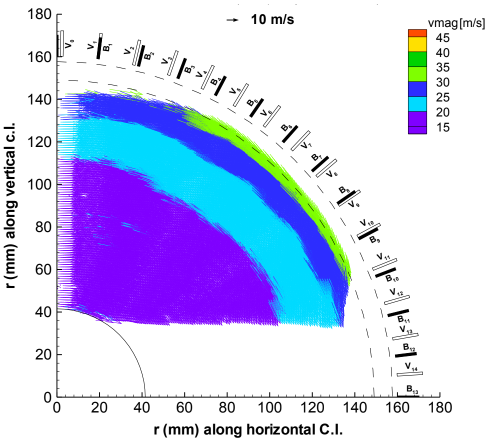

(b) $x = 10.2$ mm

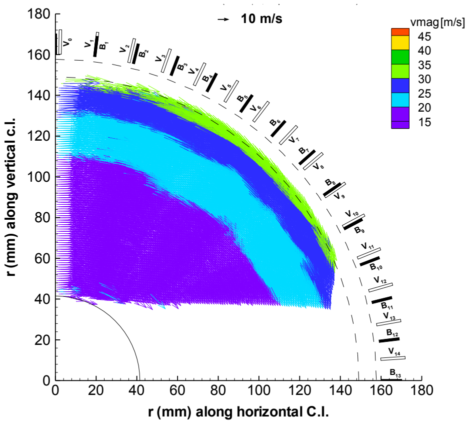

(c) $x = 7.1$ mm

Figure 28. Experimental PIV measurements - ensemble average of 10 instantaneous fluid velocity maps

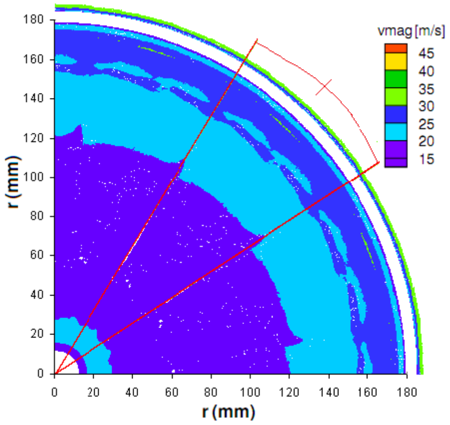

(a) $x = 14.5$ mm

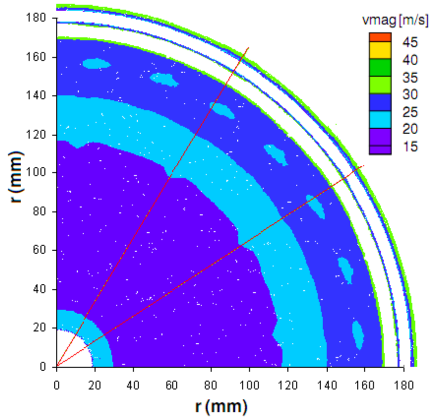

(b) $x = 10.2$ mm

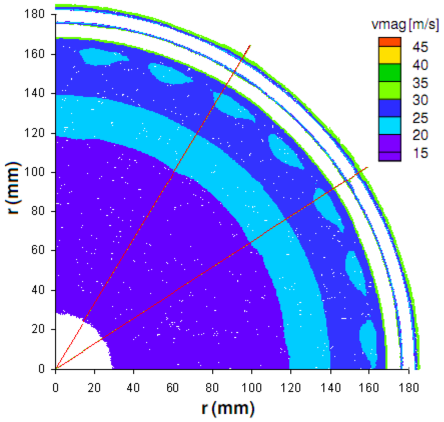

(c) $x = 7.1$ mm

Figure 29. Steady simulation (MESH I) fluid velocity magnitude.

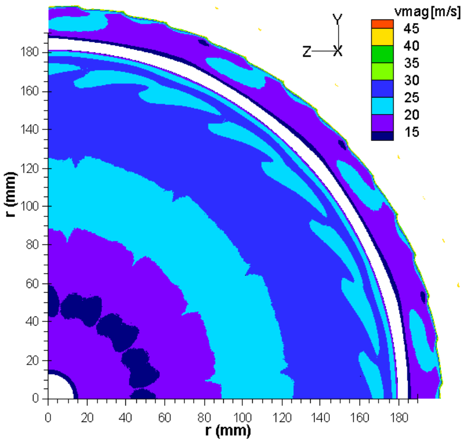

(a) $x = 14.5$ mm

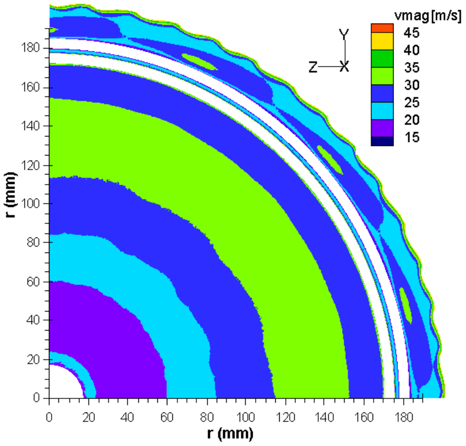

(b) $x = 10.2$ mm

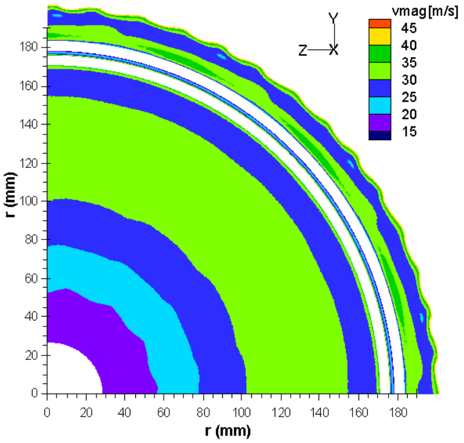

(c) $x = 7.1$ mm

Figure 30. Unsteady simulation (MESH II) mean fluid velocity magnitude.

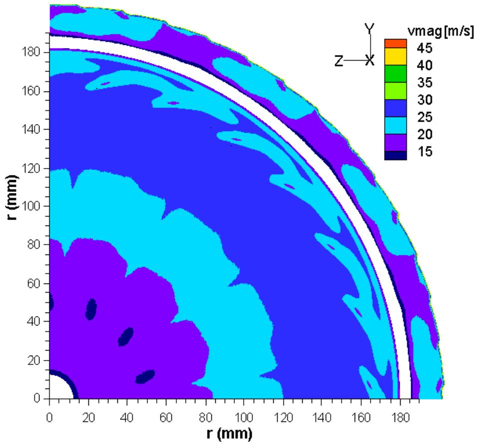

(a) $x = 14.5$ mm

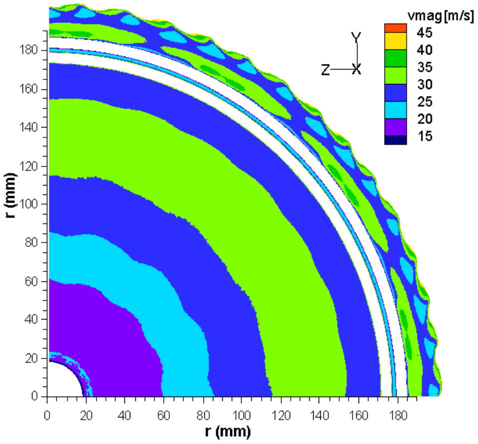

(b) $x = 10.2$ mm

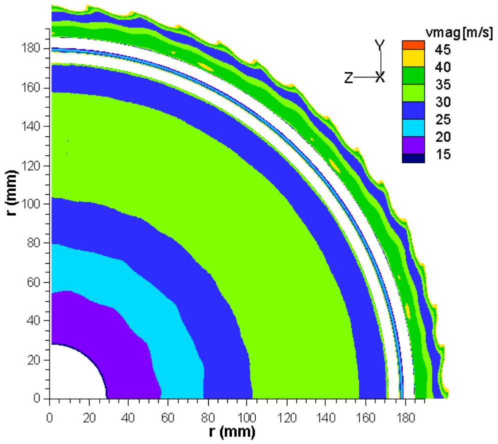

(c) $x = 7.1$ mm

Figure 31. Unsteady simulation (MESH II) instantaneous fluid velocity magnitude.

Optical visibility is restricted to the radius range between $40 \geq r \geq 150$ mm because of the inner rotor hub and and the radially outboard pre-swirler. Closest to the stator surface is the $x = 14.5$ mm plane shown in Figure 28(a), but all three planes exhibit a very similar trend. Figures 29-31 in the $x = 14.5$ mm plane show the pre-swirled purge air flow-structures at $r \cong 160$ mm. Notably, the imparted tangential velocity of the purge flow is larger than the the surrounding indigenous cavity air near the stator. The PIV maps can only resolve the tangential and radial velocity components because the camera viewing direction is orthogonal to the r-φ plane. The tangential velocity component is dominant in this swirling flow - the axial component is at most approximately 1/10th as large as the tangential; hence, these velocity maps depict a fairly accurate total vector magnitude.

$$\upsilon_t \gg \upsilon_r \geq \upsilon_x \tag{78}$$

The simulation results display all cells within the contour velocity range (15-45 m/s) in Figures 29-31 and are expressed relative to a non-moving frame, i.e. the stator walls. The cavity has one giant vortex swirling clockwise about the x-axis in the r-φ plane. Because of the no-slip conditions at the walls, a high velocity ($\upsilon_\varphi = r\omega$) is seen surrounding the rotor seal ring wall and a zero velocity at the stator seal ring. This creates a very large velocity gradient $\frac{d\upsilon_\varphi}{dr}$ between the seals.

The results of MESH I (Figure 29) appear to under-predict the experimental velocities, but are qualitatively similar. Conversely, the MESH II results (Figures 30 and 31) over-predict the experimental velocities farther from the cavity wall, while lower-than-experimental velocities exist near the wall. In Figures 31(a-c), unsteady effects of the vane/blade interaction are more noticeable radially outboard of the seals where the instantaneous velocities are larger than the averages in all three planes. Additionally, flow structures with a length scale of four vane pitches are captured within the periodic section, confirming that the approach of including extra vane pitches is a worthwhile undertaking. Further research is warranted in modeling a sector of even greater angle, as these larger flow structures may also be significant factors of ingestion.

1. Circumferential Averages

Another comparison can be made by plotting the circumferential arithmetic-average $\left(\frac{1}{25.7^\circ}\int_{0^\circ}^{25.7^\circ} \upsilon d\varphi\right)$ of the velocity data along the radial coordinate. This reduces the dimension by one, and all three r-φ planes fit on one graph. Radial and tangential velocities are computed from the PIV images and compared against the simulations in Figures 32 and 33.

From Figure 32, it becomes apparent that the steady-state simulations predict radial velocities tangibly different from the experiment. In fact, the steady-state solutions predict small negative radial velocities at each of the three axial locations while the experiments show small positive radial velocities. MESH II also initially behaved similarly to MESH I, but once the solution transitioned into an unsteady-state, the radial velocities became more positive and more closely matched the ex-

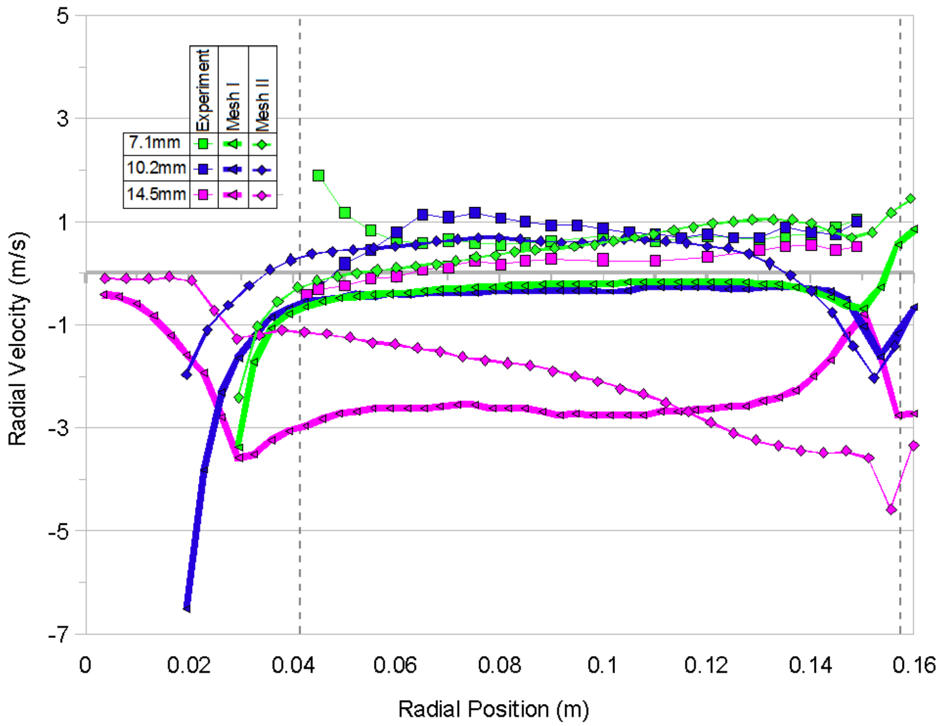

Figure 32. Comparison of circumferential-averaged radial velocity V_r at various axial locations x: Experimental (Ensemble average), MESH I, and MESH II (Instantaneous)

perimental measurements. The physical explanation is that the center of the vortex in the r-x plane moved closer to the stator cavity wall.

Radial velocities from the PIV results don't offer compelling evidence to their accuracy,. Radial velocities should be positive at the rotor wall because of the disk pumping effect (centrifugal accelerations) and the overall volumetric flow rate must be "negative" because the net flow moves radially inward toward the purge flow exit. Bricaud *et al.*[21] confirms this "pumping effect" with PIV measurements in a pre-swirled purge air cavity flow. The flow rate through any surface of fixed

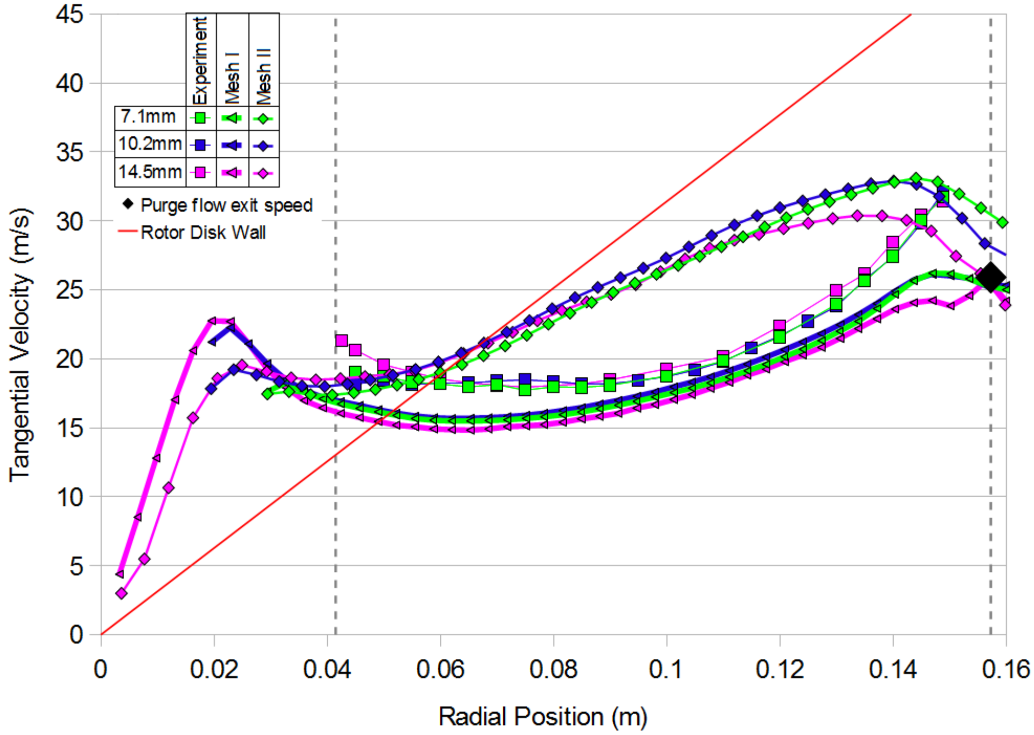

Figure 33. Comparison of circumferential-averaged tangential velocity V_φ at various axial locations x: Experimental (Ensemble average), MESH I, and MESH II (Instantaneous)

radius can be described by Equation (79).

$$Q = \int_{0mm}^{16.5} \int_{0^\circ}^{25.7^\circ} v_r \, d\varphi dx < 0 \qquad (79)$$

Therefore the simulation results showing negative radial velocities near the stator wall agrees with the physical interpretation where the cavity consists of one vortex rotating clockwise in the r-x plane. In retrospect, the time interval between the laser pulse pair employed in the PIV experiments (15-20 μs) may not have been optimal for resolving the small radial velocities. Future experiments should use a lower pulse time. The variation between the results from MESH I and MESH II can be attributed to r-x plane vortices with different centers axially.

Nearly identical negative radial velocities were predicted in MESH I and II nearest the stator wall at $x = 14.5$ mm (Figure 32) during the steady-state stage. MESH I had been refined such that $y^+ < 4$ was imposed on the cavity walls, whereas MESH II had $y^+ < 15$. Nonetheless, velocity profiles near the stator wall appeared nearly identical for the two varying turbulence models, wall functions, and meshes. The two simulation results differed farther from the wall at $x = 10.2$ mm and $x = 7.1$ mm. Where MESH I predicts lower radial velocities ($-1 < V_r < 0$) and MESH II predicts larger magnitudes ($-4 < V_r < -2$ m/s). No ingestion occurred in MESH I and velocity vectors were always oriented radially outward through the seal.

Conversely, tangential velocity components match the experimental data very closely for MESH I, as shown in Figure 33. Note that any velocities above the "rotor disk wall" speed velocity indicate "over-swirl" and velocities below exhibit "under-swirl." MESH II yields similar profiles, but the velocities over-predict the experimental data, especially at larger radial positions near the pre-swirler. This could possibly be caused by the different turbulence model (k-ϵ) employed in MESH II. The pre-swirled jets entering the cavity are generating turbulence, affecting the calculated velocities differently than the S-A model would. Notably, all axial locations accurately match the estimated tangential velocity at the pre-swirler exit ($r = 160$ mm). This estimation plotted in Figure 33 was calculated by dividing the volumetric purge flow rate by the area of the pre-swirl nozzles and accounting for the incident angle of 10 degrees. Considering that the boundary conditions for the purge inlet were set upstream of the pre-swirler nozzle and the flow was accurately predicted at the nozzle exit after having flowed through the complex pre-swirler geometry is substantial. However, it should be noted that the experimentally measured velocities are the furthest from matching the nozzle exit velocity.

B. Pressure Taps

Pressure taps were placed on non-moving walls to measure the air pressure inside the turbine rig experimental setup. Figure 1 shows all of the locations marked with the letter P. The ones located on the stator wall were all at the same azimuthal angle and varied only in radial position. Conversely, the pressure taps on the outer shroud were all at the same radial distance, but were equally spaced over a 12 degree azimuthal range as shown in Figure 3. Comparisons are made between the experiment and simulations in this section.

1. Stator Wall

One pressure tap is located just radially outboard of the seals ($r = 187$ mm), one between the seals ($r = 177$), and four more locations within the cavity ($r < 171$ mm). Figure 34 shows the experimental measurements from these pressure taps. Mean pressure ($\overline{p}$) results are shown for MESH II. The simulation data has been biased by a constant pressure value to more clearly demonstrate static pressures relative to the experiment in the figure. Both the steady and unsteady meshes predict the pressure results accurately across the entire disk radial distance. Overall, the pressure differential across the entire cavity in the radial direction is slightly less than the measured value for both meshes.

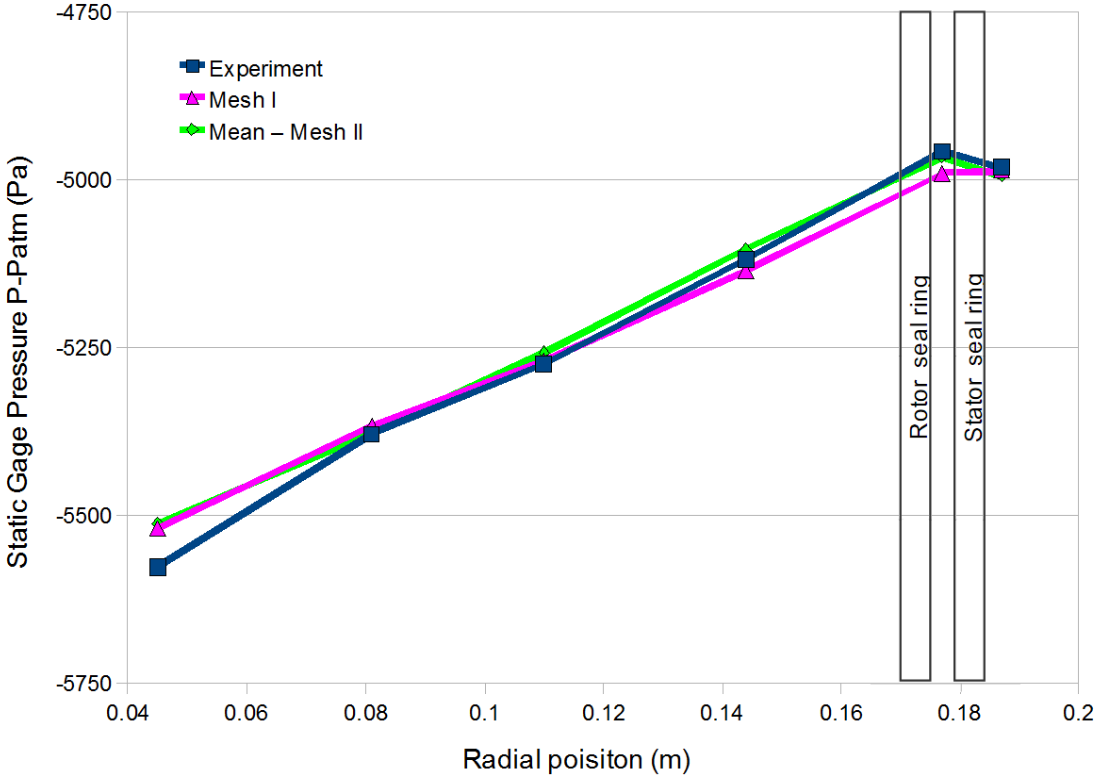

Figure 34. Comparison of static pressure radial distribution at the stator surface

2. *Outer Shroud*

Static pressure measurements at the outer shroud of the turbine stage 1 mm downstream of the vane trailing edge over a 12 degree azimuthal angle are compared to the simulation results in Figure 35. The number of vanes in the experimental (59) setup and the simulation (56) are similar enough that a comparison can be made using the same angular coordinates in Figure 35. The MESH II instantaneous pressure has been biased by a constant value to simplify comparisons with the experimental pressures. In accordance with the PIV experimental procedure, the instantaneous results from MESH II are taken at the instant the vane and blade were aligned similar to Figure 8. The circumferential pressure distribution shows some symmetry across each pitch of the vanes, but slight asymmetries suggest that a larger flow structure exists within the domain, though they may also be caused by slight difference in the mesh between vane pitches. A single vane pitch sector simulation would not be capable of capturing this flow feature.

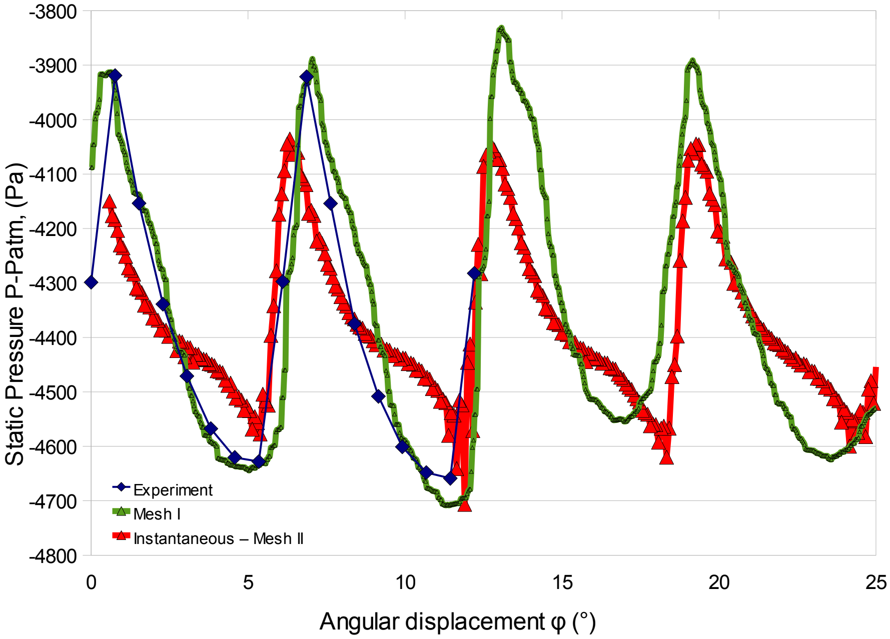

Figure 35. Circumferential distribution of static pressure at the outer shroud 1 mm downstream of the vane trailing edge

The pressure profiles found here match similarly to those simulations performed by Green *et al.*[29]

C. Concentration

Finally, results available from the CO_2 tracer gas concentration measurements along the stator surface are addressed. The concentration tap locations are shown in Figure 1. The sealing effectiveness defined in Equation 80 is plotted for the experimental data in Figure 36.

$$\zeta(r) = \frac{C(r) - C_{main}}{C_{purge} - C_{main}} \tag{80}$$

The sealing effectiveness of 0.23 at $r/b = 0.928$ (i.e., $r = 187$ mm) indicates that some of the outgoing purge air egressed to that region of the stator surface. Likewise, the sealing effectiveness of 0.84 at $r/b = 0.878$ ($r = 177$ mm) suggests mixing locally between the outgoing purge air and the incoming main air (ingestion). At the time of this writing, the simulated CO_2 concentration in MESH II has not propagated through the fluid sufficiently to accurately calculate the sealing effectiveness.

D. Simulation Predictions

The simulation offers supplemental data that was not measured or was impossible to measure in the experiments. Many velocity vector and pressure plots were acquired throughout the simulation process. Flow fields through the seal rings and cavity vortices in the r-x plane are observable from the simulation data and provide some useful insight on the mixing between the purge, cavity, and mainstream air. For comparison with previous works such as,[2,13] Figures 37 and 39 display velocity

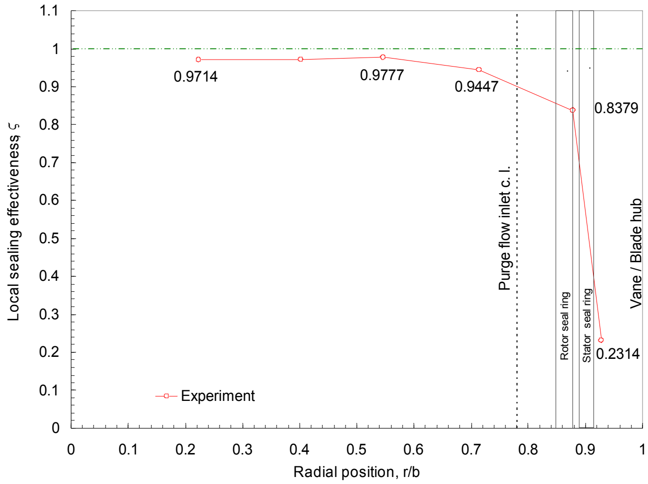

Figure 36. Experimental sealing effectiveness

magnitude vectors projected onto the r-x plane near the seal region for both meshes. In Figure 37 the plane is located at the bisection azimuthally ($\varphi = 12.9^\circ$) of the sector, and the drawn vector density is reduced to facilitate flow visualization. MESH I uses an unstructured grid everywhere, but when compared to MESH II, exhibits very similar flow recirculation within the seals. In hindsight, 40 cells radially across the seal ring gap in MESH II may be more than necessary because the $y^+ < 1$ was satisfied on the seal ring walls and 400 circumferentially across is also sufficient. Early in the simulation just shortly after a steady-state solution had been reached, the seal gap showed a fully developed flow depicted in Figure 38. As expected, no ingestion had occurred, and will not occur for the selected purge rate in a steady-state case. Numerous previous studies have arrived at the same conclusion about steady-state models.

Both meshes predicted positive radial velocities along the rotor wall inside the

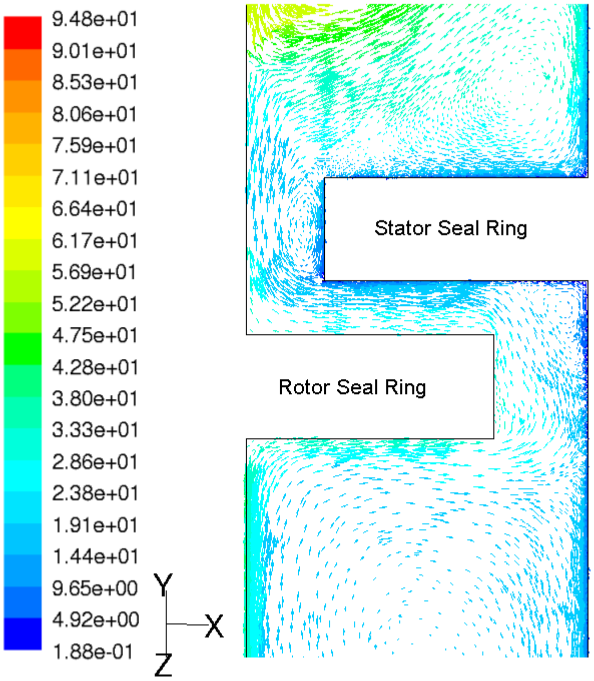

Figure 37. Vectors of velocity magnitude (m/s) projected onto the r-x plane at $\varphi = 12.9°$ near the seal region of MESH I

cavity. MESH II (Figure 39) uses a structured grid in the narrowest region near the protruding seals. Furthermore, the boundary between the moving and non-moving fluid volumes is shown in Figure 39 (dashed line) i.e., the dashed line is the sliding interface. MESH I did not model an unsteady case and hence does not include a sliding interface.

Unsteady effects are very noticeable by observing the velocity field in the seal region. The steady-state solutions also predicted flow separation at the seal ring's abrupt edges. As the unsteady simulation progressed further, these small flow separations often transformed into larger recirculation patterns as shown in Figure 39(a) within the stator seal ring's axial clearance. Occurrences of these patterns var-

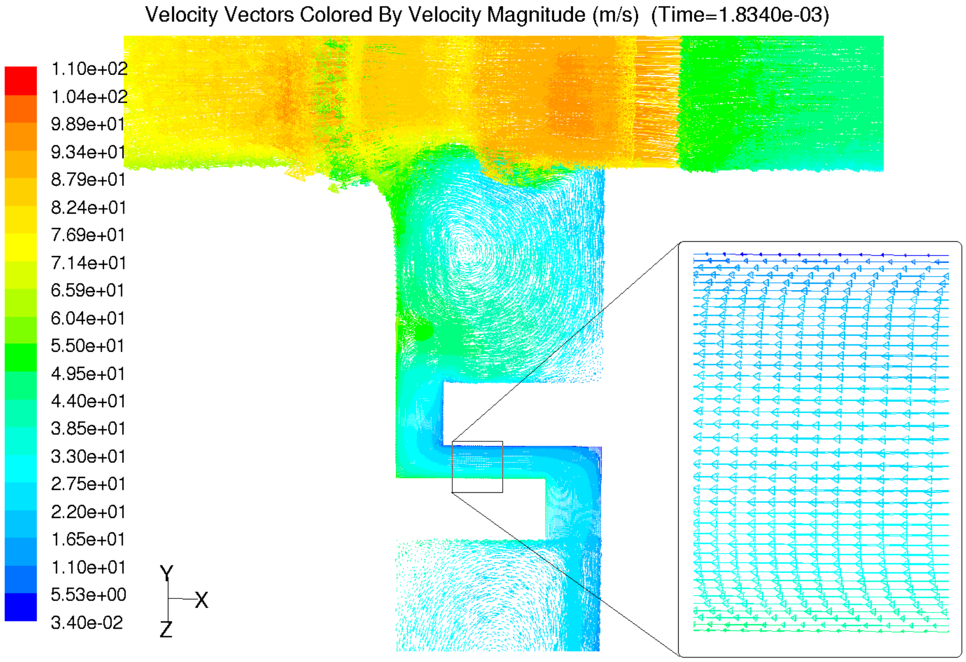

Figure 38. MESH II - Fully developed flow between seals during initial steady-state simulation

ied circumferentially for any single time instant as observed when comparing Figures 39(a) and (b), which show velocity fields for a *single* time instant at two different circumferential angles. These recirculation patterns act as a mechanism in which mainstream air can be ingested. The vortex radially inboard of the stator seal against the stator wall was always present; MESH I included.

Within the cavity, the main vortex rotates about the x-axis, but a secondary vortex exists in the x-r plane due to the "pumping effect" of the turbine disk, and many smaller vortices are apparent within the seal gap from flow separation. The rotor disk acts as a centrifugal pump, forcing fluid along the disk wall radially outward and creates the secondary vortex inside the cavity. This pumping mechanism mixes the cooling flow, and has been observed by Zerelli *et al.*[3] to be much more dominant

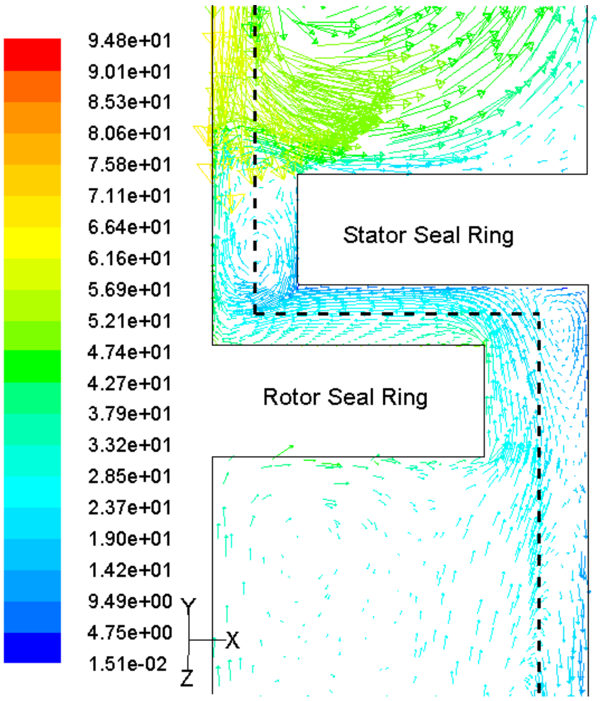

(a) $\varphi = 12.9°$

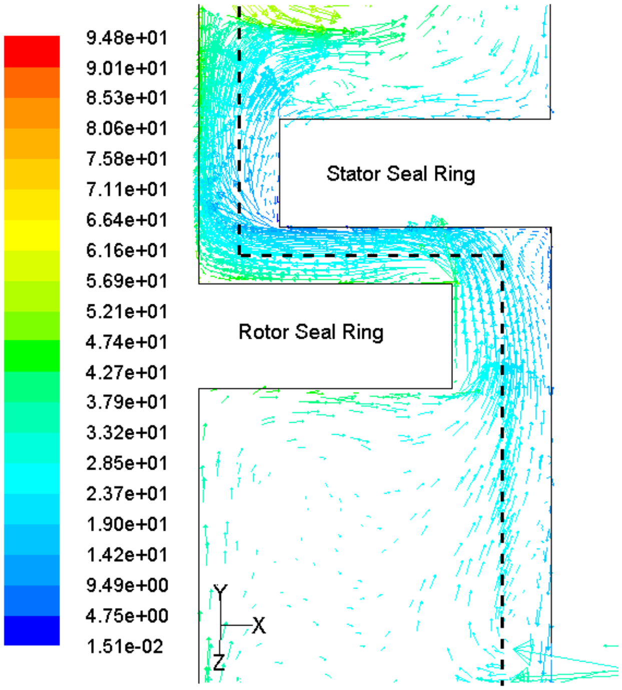

(b) $\varphi = 22.9°$

Figure 39. Instantaneous vectors of velocity magnitude (m/s) projected onto the r-x plane near the seal region (MESH II). Dashed line indicates the sliding interface boundary

than natural convection effects.

Figure 39(a) shows high negative radial velocities near the rotor wall radially outboard of the seal rings. These velocities are due to the high pressure at the leading edges of the rotor blades, forcing the mainstream air radially inward toward the seal rings. It is expected that these large negative radial velocities may grow and cause the air to become entrained with the smaller vortex between the stator seal ring's axial clearance. Eventually the mainstream air will move into the radial clearance, moving horizontally along the underside of the stator seal ring wall. Once traversing horizontally across the entire axial overlap, the air should reach the vortex located within the rotor seal ring's axial clearance ($x \cong 16$ mm) and be directed radially inward along the stator wall and into the cavity. However, more iterations are needed to reach a conclusive answer of whether ingestion occurs in this unsteady sector model. Zhou *et al.*[6] required at least 120 blade pitch passing cycles to achieve a temporally periodic solution of sealing effectiveness, and the present work only achieved around 20. It was seen that the CO_2 slowly progressed through the unsteady vortices that formed, and this explains why so many blade pitch passings are required.

Lastly, but most importantly, time-animations of the unsteady flow in the region between the blades and vanes revealed a very significant ingestion mechanism. Because this region was expected to be critical in the unsteady case, MESH II was made fine enough such that 3.5 million cells existed in that region alone, plus another one million between the seal rings. Refining this region proved worthwhile for resolving vortices that appear to be the main cause of ingestion. As many previous works have claimed, the predominant cause of ingestion is known to be the three-dimensional unsteady flow field that exists in the main gas path of the turbine stage.[2,6–9] Not only does the present work confirm this, it also offers further explanation. Because the egressed gas from the seal rings is moving slower tangentially (υ_t), a high velocity gradient $\frac{\partial \upsilon_t}{\partial r}$ exist between the blades and seal rings.

Observing the modeled CO_2 concentration provides an excellent method of tracing the general particle paths through these unsteady structures, especially when viewed in a r-φ plane. Shearing and momentum transfer occur between the egressed and mainstream gases, and the blades/vanes presence places non-uniform circumferential pressure perturbations upon this mixing layer. These spatial oscillations of the mixing layer can be seen initially in CO_2 concentration plots in the form of a sine wave pattern, even in the steady-state model. But, no further mixing occurs until the unsteady time-dependent model is solved and the unstable perturbations in the layer cause the waves to collapse after a certain time. Thus, the high speed mainstream gas becomes entrained and pushed radially inward toward the seal gap. Indigenous cavity gas is conversely pulled radially outward from that same vortex mixing. Figure 40 shows the time evolution of the CO_2 concentration and theses mixing vortices that help enable ingestion. The final time of $t = .010532$[s] occurs at more than half of a disk rotation (30 blade passings). It should also be mentioned that these “waves” at the mixing layer, travel about half as fast as the rotor disk wall speed, and that the wavelength of the waves is not necessarily one blade pitch, as

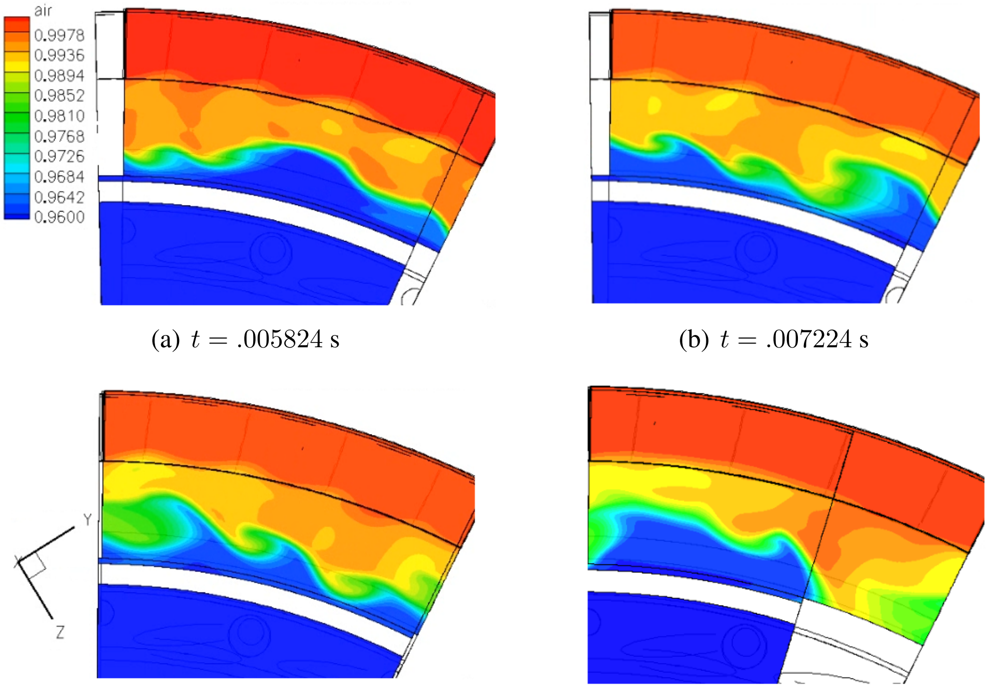

(a) $t = .005824$ s (b) $t = .007224$ s

(c) $t = .008589$ s (d) $t = .010532$ s

Figure 40. MESH II - time-evolution of air mass fraction through unsteady vortices in r-φ plane at $x = 2$ mm

some of the waves can merge together and produce constructive interference to further promote ingestion by creating larger vortices. Modeling a larger sector angle would be highly beneficial for future work.

Once the mixed mainstream air has protruded radially inward and reached the rotor seal ring, it must next traverse through the radial seal gap. Figure 41 demonstrates the onset of this migration by showing large positive axial velocities along the rotor seal ring wall that guide the mainstream air through the radial gap. In fact, the vortices of the velocity field in Figure 41(a) show a path for the mainstream air to reach the cavity. This was the furthest time step reached by the simulation at the time of this writing. Ingestion will only occur under the precise circumstances in

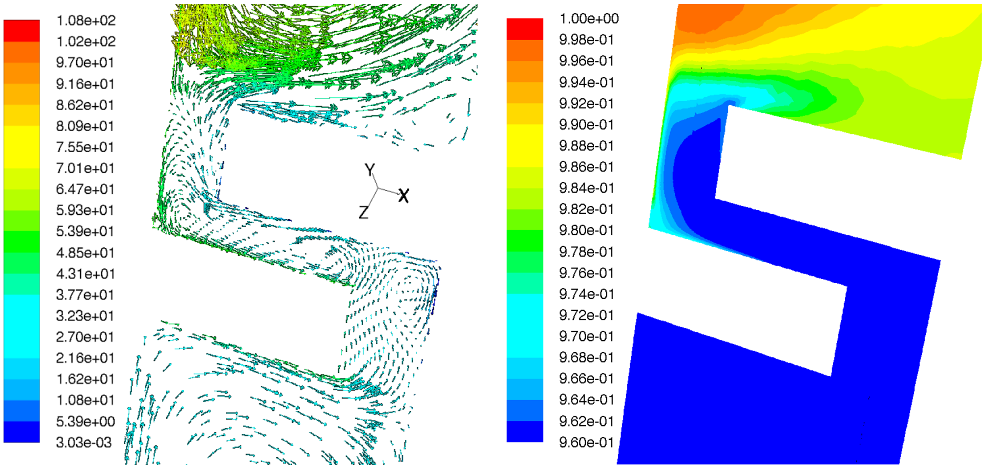

(a) Velocity magnitude (m/s) vectors (b) Air mass fraction contours

Figure 41. MESH II - Onset of ingestion axially through the seal rings at $\varphi = 12.9°$ and $t = .010532$ s

which all of the various unsteady vortices throughout the different seal ring regions, described previously, allow for a complete particle path through the seal rings and into the cavity. And though it has not yet occurred in the present simulation, convicing evidence from Figure 41 and Murphy's Law would dictate that given more computational time, the proper circumstances may become present.

IX. Summary

Using experiments and simulations to help understand the flow field in a turbine rotor-stator cavity and the ingestion of mainstream gas into the cavity has proven to be insightful. Much knowledge has been gathered in terms of properly setting up the procedures for modeling and data acquisition as well as the data itself.

Some major obstacles were overcome during the computational model design phase. It was learned that the modeled geometry should be designed to avoid locations that generate highly skewed cells, such as the blades and vanes being flush with the end wall edges. Changes can be made to the grid without greatly modifying the geometry and can simplify the meshing procedure. For periodic sections, it is critical to keep the mesh similar in the circumferential direction, i.e. cell volumes should adhere to the general rule $\frac{\partial V}{\partial \varphi} = 0$. Employing pressure boundary conditions instead of mass flow rates is also desirable for inlet/outlet boundaries.

Experimental measurements were used as a baseline to assess how well the CFD model could predict the flow fields. Fluid velocity, static pressure, and tracer gas concentration measurements offered some insight to the actual flow field, and the equivalent data was extracted from the simulations for comparison. These comparisons of results have been reported for two meshes with an identical turbine stage geometry against actual experimental measurements with a similar turbine stage geometry. Three-dimensional, second-order spatial accuracy was used on the rotationally periodic 25.71 degree sector (1/14th of the annulus) containing four vanes and four blades. Varying factors in the mesh and CFD solver parameters have resulted in two unique but similar solutions. Both simulations show general agreement with the experimental measurements of radial velocity, tangential velocity, and static pressure distributions.

MESH I used a steady-state solver and a simpler turbulence model, but it nevertheless predicted pressure distributions and tangential velocities within the cavity quite accurately. MESH I did not show any ingestion, but this was expected as seen in many previous works. Instead, MESH I results were exploited to design a subsequent improved MESH II for an unsteady simulation. Solutions obtained from MESH II exhibited unsteady effects, especially within the seal gap and regions influenced by blade/vane interactions. Mainstream air penetrated significantly farther into the seal rings than with the steady-state case, but still did not fully ingress into the cavity. It is highly likely that this would eventually occur given more time for the exact circumstances to occur so that mainstream air may be carried through the seal rings. Small unsteady perturbations can produce large instabilities and flow structures that may lead to ingestion. The longer the simulation runs, the higher the possibility that a suitable unsteady perturbation would occur. A time-dependent simulation is crucial in accurately predicting ingestion. Non-uniform circumferential pressure perturbations from the blades and vanes caused the mixing layer to become unstable. Vortices formed as a result of the mixing layer collapsing during the transition from a steady-state to a time-periodic solution, and this is believed to be the major cause of ingestion based on the present findings.

Larger flow structures spanning across the entire sector were also realized. Further research is warranted in expanding the sector angle to include even more vane pitches. A simulation of the complete 360 degree model using mesh resolution comparable to that applied here should provide additional insight to the unsteady flow field, especially regarding the large scale structures that are likely significant contributors to ingestion. A rotational periodicity simplifying assumption restricts the size of the largest realizable flow structures.

Future work may also benefit from measuring temperatures of heated inlet air and also modeling temperature distributions through the fluids and solid walls.[3] Cooling and heat transfer at the turbine wall could be monitored and the effects of turbulent mixing inside the cavity could be explored for various purge flow inlet geometries[15] as well as provide another means of measuring sealing effectiveness.

Many previous papers, especially steady cases, focused solely on the spatial grid resolution, and refining it. However, it is necessary to realize that with an unsteady case, using a proper temporal resolution is just as important. Unsteady cases, as the one performed in the current work, are very computationally demanding and may prove to be even more insightful as computational power becomes faster and cheaper.

References

[1] Fluent Inc. 12.4.3, *FLUENT 6.3 Users Guide.*, 2006.

[2] Roy, R. P., Xu, G., Feng, J., and Kang, S., “Pressure Field and Main-Stream Gas Ingestion in a Rotor-Stator Disk Cavity,” ASME paper 2001-GT-564, 2001.

[3] Zerelli, N., “Analysis of a Turbine Rim Seal Cavity Via 3D-CFD Using Conjugated Heat Transfer Approach,” AIAA paper 092407, 2008.

[4] Khilnani, V. I., Tsai, L. C., Bhavnani, S. H., Khodadadi, J. M., Goodling, J. S., and Waggott, J., “Mainstream Ingress Suppression in Gas Turbine Disk Cavities,” *ASME J. Turbomachinery*, Vol. 116, 1994, pp. 339 – 346.

[5] Daniels, W. A., Johnson, B. V., Graber, D. J., and Martin, R. J., “Rim Seal Experiments and Analysis for Turbine Applications,” *ASME J. Turbomachinery*, Vol. 114, 1992, pp. 426 – 432.

[6] Zhou, D.-W., Roy, R. P., Wang, C., and Glahn, J., “Main Gas Ingestion in a Turbine Stage for Three Rim Cavity Configurations,” ASME paper GT2009-59851 (to appear in ASME J. Turbomachinery, 2010)., 2009.

[7] Teramachi, K., Hamabe, M., Manabe, T., and Yanagidani, N., “Experimental and Numerical Investigation of Sealing Performance of Turbine Rim Seals,” IGTC2003tokyo TS-025, 2003.

[8] Cao, C., Chew, J., Millington, P., and Hogg, S., “Interaction of Rim Seal and Annulus Flows in an Axial Flow Turbine,” ASME paper GT-2003-38368, 2003.

[9] Roy, R. P., Feng, J., Narzary, D., and Paolillo, R., “Experiments on Gas Ingestion Through Axial-Flow Turbine Rim Seals,” *ASME J. Engineering for Gas Turbines and Power*, Vol. 127, 2005, pp. 573 – 582.

[10] Wang, C.-Z., Johnson, B. V., Cloud, D. F., Paolillo, R. E., Vashist, T. K., and Roy, R. P., “Rim Seal Ingestion Characteristics for Axial Gap Rim Seals in a Closely-Spaced Turbine Stage From a Numerical Simulation.” ASME paper GT2006-90965, 2006.

[11] Jakoby, R., Zierer, T., Lindbald, K., Larsson, J., deVito, L., Bohn, D., Funcke, J., and A.Decker, “Numerical Simulation of the Unsteady Flow Field in an Axial Gas Turbine Rim Seal Configuration,” ASME paper GT2004-53829, 2004.

[12] Hills, N. J., Chew, J. W., and Turner, A. B., “Computational and Mathematical Modeling of Turbine Rim Seal Ingestion,” *ASME J. Turbomachinery*, Vol. 124, 2002, pp. 306 – 315.

[13] Roy, R. P., Zhou, D.-W., Ganesan, S., Wang, C.-Z., Paolillo, R., and Johnson, B., "The Flow Field and Main Gas Ingestion in a Rotor-Stator Cavity." ASME paper GT2007-27671, 2007.

[14] Dunn, D. M., Zhou, D.-W., Saha, K., Squires, K. D., Roy, R. P., Kim, Y. W., and Moon, H. K., "Flow Field in a Single-Stage Model Air Turbine Rotor-Stator Cavity with Pre-Swirled Purge Air Flow." ASME paper GT2010-22869, 2010.

[15] Okita, Y., Nishiura, M., Yamawaki, S., and Hironaka, Y., "A Novel Cooling Method for Turbine Rotor-Stator Rim Cavities Affected by Mainstream Ingress," *ASME J. Engineering for Gas Turbines and Power*, Vol. 127, 2005, pp. 798 – 806.

[16] Gentilhomme, O., Hills, N. J., Turner, A. B., and Chew, J. W., "Measurement and Analysis of Ingestion Through a Turbine Rim Seal," *ASME J. Turbomachinery*, Vol. 125, 2003, pp. 505 – 512.

[17] Paniagua, G., Dènos, R., and Almeida, S., "Effect of the Hub Endwall Cavity Flow on the Flow-Field of a Transonic High-Pressure Turbine," *ASME J. Turbomachinery*, Vol. 126, 2004, pp. 578 – 586.

[18] McLean, C., Camci, C., and Glezer, B., "Mainstream Aerodynamic Effects Due to Wheelspace Coolant Injection in a High-Pressure Turbine Stage: Part I Aerodynamic Measurements in the Stationary Frame," *ASME J. Turbomachinery*, Vol. 123, 2001, pp. 687 – 696.

[19] McLean, C., Camci, C., and Glezer, B., "Mainstream Aerodynamic Effects Due to Wheelspace Coolant Injection in a High-Pressure Turbine Stage: Part II Aerodynamic Measurements in the Rotational Frame," *ASME J. Turbomachinery*, Vol. 123, 2001, pp. 697 – 703.

[20] Denton, J. D. and Dawes, W. N., "Computational Fluid Dynamics for Turbomachinery Design." *Proc. IMechE Part C*, Vol. 213, 1999, pp. 107 – 124.

[21] Bricaud, C., Richter, B., Dullenkopf, K., and Bauer, H.-J., "Stereo PIV Measurements in an Enclosed RotorStator System with Pre-Swirled Cooling Air," Experiments in fluids (2005) 39: 202-212, Springer-Verlag, 2005.

[22] Bernard, P. S. and Wallace, J. M., *Turbulent Flow Analysis, Measurement, and Prediction*, John Wiley and Sons Inc., Hoboken, New Jersey, 2002.

[23] Kundu, P. K., *Fluid Mechanics*, Acedemic Press, Inc., San Diego, CA 92101, 1990.

[24] Panton, R. L., *Incompressible Flow*, John Wiley and Sons Inc., Hoboken, New Jersey, 3rd ed., 2005.

[25]Boydston, J. D., *"Detached Eddy Simulation of High Reynolds Number Flow Over a Rectangular Cavity"*, Master's thesis, Arizona State University, USA, May 2008.

[26]Davidson, P. A., *Turbulence an Introduction for Scientists and Engineers*, Oxford University Press, Great Claredon Street, Oxford OX 2 6DP, 2004.

[27]He, J., *Numerical Simulation of Turbulent Flow and Thermal Fields in a Rotor-Stator Cavity with External Flow*, Master's thesis, Arizona State University, USA, August 1999.

[28]Montomoli, F., Massini, M., Maceli, N., M.Cirri, Lombardi, L., Ciani, A., DErcole, M., and DeProsperis, R., "Interaction of Wheelspace Coolant and Main Flow in a New Aeroderivative Low Pressure Turbine," *ASME J. Turbomachinery*, Vol. 132, 2010, pp. 031013–1.

[29]Green, B. R., Barter, J. W., Haldeman, C. W., and Dunn, M. G., "Averaged and Time-Dependent Aerodynamics of a High Pressure Turbine Blade Tip Cavity and Stationary Shroud: Comparison of Computational and Experimental Results," *ASME J. Turbomachinery*, Vol. 127, 2005, pp. 736 – 746.

APPENDIX A.

Figure 42. Power plant gas turbine using axially overlapping seal ring configuration